39.1 (sec.), 42.8 (sec.), 51.8 (quat.), 52.2 (tert.), 54.8 (tert.), 61.5 (quat.), 64.5 (quat.), 67.0 (tert.), 75.5 (quat.), 136.0 (olefinic), 139.3 (olefinic), 141.3 (olefinic), 144.1 ppm (olefinic.); MS (FAB, *m/z*) 294 [M$^+$]. Anal. Calcd for $C_{21}H_{26}O\cdot 1/4H_2O$: C, 84.37; H, 8.85%. Found: C, 84.49; H, 8.85%. **25**: colorless crystals (toluene), mp 69−71 °C; ^{1}H NMR δ 1.20 (d, J = 12.0 Hz, 1H), 1.28 (s, 1H), 1.35 (s, 1H), 1.41 (d, J = 12.0 Hz, 1H), 1.44−1.71 (m, 13H), 1.78−1.81 (m, 1H), 1.88−1.94 (m, 2H), 1.99−2.02 (m, 2H), 2.04 (d, J = 6.5 Hz, 1H), 2.06 (s, 2H), 2.14 (d, J = 6.5 Hz, 1H); ^{13}C NMR (DEPT) δ 19.5 (sec.), 29.4 (sec.), 30.4 (sec.), 35.4 (sec.), 36.4 (sec.), 36.8 (sec.), 37.8 (two sec.), 38.3 (tert.), 39.3 (sec.), 40.1 (sec.), 43.1 (quart.), 43.3 (quart.), 46.0 (tert.), 47.1 (tert.), 50.8 (tert.), 55.8 (quat.), 56.0 (quat.), 58.5 (quat.), 62.7 (tert.), 77.0 (quat.); MS (FAB, *m/z*) 294 (M$^+$). Anal. Calcd for $C_{21}H_{26}O\cdot 1/2H_2O$: C, 83.12; H, 8.97%. Found: C, 83.16; H, 8.94%.

(3) Photolysis of 2 in a Mixture of MeOH and 2 mol/L Aqueous HCl (17:1, v/v). A MeOH-2 mol/L HCl (17:1, v/v) solution (270 mL) of **2** (760 mg, 2.74 mmol) in a quartz vessel was irradiated with sterilizing lamps (10 W × 7) under Ar for 80 min at room temperature while monitoring the reaction by the ^{1}H NMR spectra in every 20 min. After removal of the solvent under reduced pressure, the residue was separated by recycle HPLC on GPC with $CHCl_3$ to afford polycyclic methoxy compound **26** (23 mg, 2.7%), polycyclic dimethoxy compound **27** (100 mg, 11%), and polycyclic methoxyhydroxy compound **28** along with the recovery of the starting **2** (80 mg, 11%). **26**: colorless oil. ^{1}H NMR δ 1.12 (d, J = 11 Hz, 1H), 1.23 (s, 1H), 2.17 (d, J = 11 Hz, 1H), 1.41−2.06 (m, 26H), 3.17 (s, 3H); ^{13}C NMR (DEPT) δ 19.9 (sec.), 30.1 (sec.), 30.9 (sec.), 33.4 (sec.), 36.2 (sec.), 37.0 (sec.), 37.1 (sec.), 37.3 (sec.), 38.4 (sec), 39.8 (sec.), 39.8 (tert.), 40.8 (sec.), 43.7 (quat.), 44.4 (quat.), 46.6 (tert.), 47.6 (quat.), 49.2 (quat.), 51.2 (tert.), 56.1 (quat.), 57.0 (quat.), 59.0 (quat.), 61.3 (prim.), 81.9 (quat.); HRMS (FAB, *m/z*) obsd. 308.2144 [M$^+$], calcd for 308.4637. **27**: mp 56−57 °C; ^{1}H NMR δ 1.03 (d, J = 13 Hz, 1H), 1.16 (d, J = 11 Hz, 1H), 1.26−1.78 (m, 20H), 1.90 (d, J = 11 Hz, 1H), 2.03 (d, J = 5.7 Hz, 1H), 2.26 (d, J = 13 Hz, 1H), 2.83 (s, 1H), 3.16 (s, 3H), 3.35 (s, 3H); ^{13}C NMR (DEPT) δ 19.9 (sec.), 25.0 (sec.), 26.1 (sec.), 32.1 (sec.), 34.0 (sec.), 35.4 (sec.), 36.5 (sec.), 36.6 (sec), 37.4 (sec.), 37.9 (sec.), 40.9 (sec.), 45.1 (tert.), 45.3 (tert.), 48.2 (quat.), 49.2 (quat.), 51.0 (tert.), 51.9 (quat.), 56.4 (quat.), 57.3 (quat.), 59.4 (prim.), 65.0 (prim.), 86.2 (quat.), 89.6 ppm (tert.). GC−MS (EI, *m/z*) 340 [M$^+$]. Anal. Calcd for $C_{23}H_{32}O_2\cdot 1/8H_2O$: C, 80.63; H, 9.39%. Found: C, 80.65; H, 9.33%. **28**: mp 138−139 °C; ^{1}H NMR δ 1.10 (d, J = 13 Hz, 1H), 1.19 (d, J = 12 Hz, 1H), 1.27−1.73 (m, 21H), 1.93 (d, J = 12 Hz, 1H), 2.07 (d, J = 4.2 Hz, 1H), 2.25 (d, J = 13 Hz, 1H), 3.18 (s, 3H), 3.32 (s, 1H); ^{13}C NMR (DEPT) δ 19.9 (sec.), 25.4 (sec.), 26.1 (sec.), 31.4 (sec.), 34.0 (sec.), 35.0 (sec.), 35.4 (sec.), 36.1 (sec.), 37.4 (two, sec.), 41.5 (sec.), 45.1 (tert.), 45.3 (tert.), 47.7 (quat.), 49.5 (quat.), 51.0 (tert.), 52.2 (quat.), 56.0 (quat.), 57.6 (quat.), 64.5 (prim.), 79.3 (tert.), 86.2 ppm (quat.). GC-MS (EI, *m/z*) 326 [M$^+$]. Anal. Calcd for $C_{23}H_{30}O_2\cdot 1/2H_2O$: C, 79.83; H, 9.28%. Found: C, 79.78; H, 9.13%

(4) Photolysis of 2 in Nonpolar Solvents. A dry hexane solution (500 mL) of **2** (700 mg, 2.52 mmol) in a quartz apparatus was irradiated with sterilizing lamps (10 W × 7) with continuous oxygen gas bubbling for 25 min at room temperature. The solvent was removed under reduced pressure, the residue was separated by PTLC (SiO_2; CH_2Cl_2), and then by HPLC (C18, MeOH). Very small amounts of **29** and **30** were isolated and identified by ^{1}H NMR and GC−MS. The yields of these compounds depend on the amount of dissolved oxygen in solution; **29** (0.8−1%) and **30** (0.6−0.7%). Irradiation of **2** (700 mg, 2.52 mmol) in acetone with high-pressure Hg lamp for 1 h gave the compounds **29** (2.7%) and **30** (1.2%) after the similar separation and purification procedure described above. **29**: yellow oil. ^{1}H NMR δ 7.01 (s, 1H), 6.78 (s, 2H), 6.65 (s, 1H), 6.37 (s, 2H), 2.54−3.12 (m, 16H); MS (FAB, *m/z*) 292 [M$^+$-H]. Anal. Calcd for $C_{21}H_{24}O$: $1.5H_2O$, C, 78.96, H, 8.52%. Found: C, 78.81, H, 8.28%. **30**: yellow oil. ^{1}H NMR δ 6.79 (s, 1H), 6.68 (s, 1H), 6.57 (s, 1H), 6.51 (s, 1H), 6.45 (s, 1H), 6.28 (s, 1H), 4.62 (s, 1H), 2.62−2.87 (m, 10H), 2.10−2.22 (m, 6H); MS (FAB, *m/z*) 291 [M$^+$]. Anal. Calcd for $C_{21}H_{22}O$: 0.65MeOH, C, 83.55; H, 7.97%. Found: C, 83.62; H, 8.01%.

(5) Photolysis of 2 in Acetone. A solution of **2** (400 mg, 1.45 mmol) in acetone (400 mL) was irradiated with a high-pressure Hg lamp (400 W) under argon for 14 h at room temperature while monitoring the reaction by ^{1}H NMR. After removal of the solvent under reduced pressure, the residue was purified by recycle HPLC on GPC type with CH_3Cl to afford 1-acetyl[3$_3$](1,3,5)cyclophane **31** (5 mg, 1.1%) along with the recovery of the starting material (114 mg, 29%). **31**: ^{1}H NMR ($CDCl_3$) δ 2.01 (s, −COMe, 3H), 2.19 (m), 2.68−2.74 (m), 3.00 (m), 6.39 (s, aromatic), 6.48−6.49 (m), 6.54−6.56 (m) ^{13}CNMR($CDCl_3$) δ 28.6, 28.8, 28.8, 30.0, 34.8, 36.8, 36.4, 36.5, 60.8, 127, 128, 130, 132, 133, 138, 140, 141, 141, 142, 208 ppm. MS (FAB, *m/z*) 332 [M$^+$], Anal. Calcd for $C_{24}H_{28}O\cdot 0.05$ benzene: C, 86.76; H, 8.48%. Found: C, 86.75; H, 8.52%.

Acknowledgment. T.S. gratefully acknowledge financial support by a Grant-in-Aid for Scientific Research (B) (No. 14340200) from the Ministry of Education, Culture, Sports, Science and Technology, Japan. T.S. sincerely thanks the financial support by the Shorai Foundation for Science and Technology, Japan.

Supporting Information Available: The alternative mechanism of single electron transfer (Scheme S1), crystal packing diagrams of compounds **24** and **31**(Figures S1, S2), and a summary of the crystallographic data and refinement details (Table S1). This material is available free of charge via the Internet at http://pubs.acs.org.

JA030032X

9-Fluoro-18-hydroxy-[3.3]metacyclophane: Synthesis and Estimation of a C–F···H–O Hydrogen Bond

Hiroyuki Takemura,*[a] Masayuki Kotoku,[b] Mikio Yasutake,[c][‡] and Teruo Shinmyozu[c]

Keywords: Hydrogen bonds / Fluorine / Cyclophanes / X-ray diffraction

A cyclophane composed of fluorobenzene and phenol units was synthesized in order to observe the C–F···H–O hydrogen bond. In the crystal structure, 20% of the molecule clearly shows the intramolecular hydrogen bond and the other 80% is free from hydrogen bonding. On the other hand, a distinct low-field shift of the phenolic OH proton was observed in the ^{1}H NMR spectrum compared to that of the F-free analog. Furthermore, O–H···F through-space coupling was observed. From the results of the crystallographic analysis, IR, and NMR spectra, the C–F···H–O hydrogen bond energy of this system was estimated to be 0.84–3.7 kJ·mol^{-1}.

Introduction

The C–F···H–X (X = O, N) hydrogen bonds are a new type of hydrogen bond, which was first proposed by Glusker et al. in 1983.[1] Following their work, research studies and discussions have been continued by many researchers who are still making efforts to confirm the hydrogen bonds using a variety of methods. This tendency indicates that CF···H–X hydrogen bonds are not widely distributed even in modern chemistry. Various methods are employed for the search, i.e., statistical methods utilizing a crystallographic database,[2,3] crystallographic analyses, spectroscopic methods,[4–9] and theoretical calculations.[10–12] Howard et al. adopted fluoromethane and fluoroethene as C–F donors and concluded that the average F···H distance of the C(sp^3)–F···H–O, C(sp^2)–F···H–O hydrogen bond is 1.9 Å using ab initio calculations.[13] They also found that examples of C–F···H–O and C–F···H–N hydrogen bonds are rare in the Cambridge Structural Database System (CSDS) and showed that the F···H–X angles are dispersed (the statistically found C–F···H–O angles are not within the certainty range). Therefore, they concluded that the interaction is weak. On the other hand, Caminati et al. observed the free jet millimeter wave spectra of the CH_2F_2···H_2O system, and concluded that the optimized distance r(F···H) = 2.20 Å and the angles ∠(F···H–O) and ∠(C–F···H) are 135 and 93°, respectively.[14]

Our studies of the C–F···M$^+$ interaction revealed that the C–F unit attracts all kinds of cations by a cation–dipole interaction as the main driving force.[15] Therefore, we can deduce that C–F can be a proton acceptor because the interaction also operates in the polarized $X^{\delta-}$–$H^{\delta+}$ (X = O, N) system.

Based on this speculation, we employed the cyclophane skeleton for investigating the C–F···H–O hydrogen bond. Phenol and fluorobenzene units in cyclophane **1** are fixed and close to each other (Figure 1). Its spectral features can be compared to those of the structurally analogous cyclophanes **2** and **3**. The C–F···H–O distance (ca. 1.9 Å) and C–F···H and F···H–O angles (ca. 99.5 and 156°) of **1** were estimated using simple molecular-model considerations. These values are close to those estimated by Howard et al. and Caminati et al. Therefore, cyclophane is thought to be an appropriate system for the observation of the C–F···H–O hydrogen bond. In this report, synthesis of the

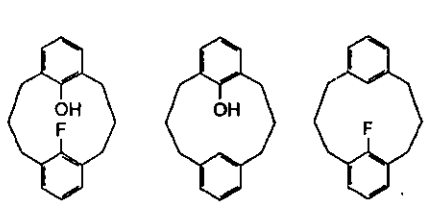

1 2 3

Figure 1. Structures of cyclophanes **1**–**3**

[a] Department of Chemistry, Faculty of Science, Kyushu University,
Ropponmatsu 4-2-1, Chuo-ku, Fukuoka 810-8560, Japan
Fax: (internat.) + 81-92-726-4755
E-mail: takemura@chem.rc.kyushu-u.ac.jp
[b] Department of Chemistry, Faculty of Science, Kyushu University,
Hakozaki 6-10-1, Higashi-ku, Fukuoka 812-8581, Japan
[c] Institute for Materials Chemistry and Engineering, Kyushu University,
Hakozaki 6-10-1, Higashi-ku, Fukuoka 812-8581, Japan
[‡] Present address: Department of Applied Chemistry, Faculty of Engineering, Saitama University,
255 Shimo-ohkubo, Sakuraku, Saitama 338-8570, Japan

Supporting information for this article is available on the WWW under http://www.eurjoc.org or from the author.

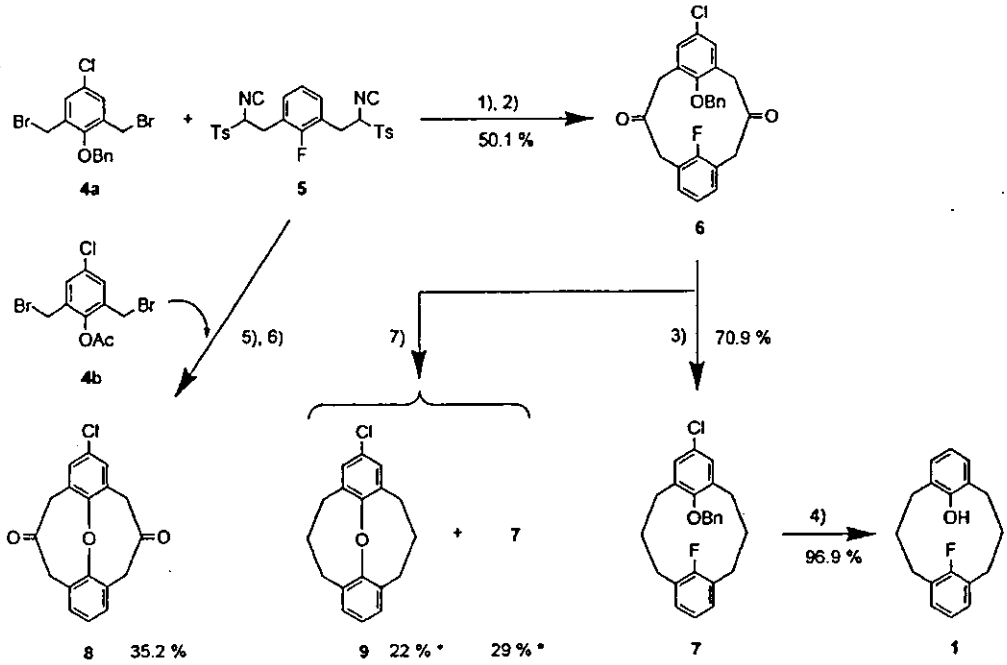

Scheme 1. Synthetic strategies of the cyclophane **1**: 1) Bu_4NI, CH_2Cl_2/aq. NaOH; 2) concd. HCl; 3) Zn/HCl (g), diethyl ether; 4) 10% Pd/C, $HCOONH_4$, MeOH; 5) NaH, DMF; 6) concd. HCl; 7) $NH_2NH_2{\cdot}H_2O$, KOH, diethylene glycol; * each yield was calculated based on the integration of signals in ^1H NMR spectrum

cyclophane, structural analysis and spectral features are discussed as one approach for investigating the C−F···H−O hydrogen bond.

Results and Discussion

Synthesis

The [3.3]metacyclophane skeleton was constracted by the TosMIC method (Scheme 1).[16] However, an unexpected ether product **8** was obtained by the initially chosen strategies employing a cyclization reaction between the acetyl-protected dibromide **4b** and TosMIC derivative **5** in DMF with NaH as the base at room temperature. This disadvantage was overcome by altering the protecting group from an acetyl to a benzyl group. The phase-transfer reaction between **4a** and **5** followed by treatment of the reaction mixture with aq. HCl afforded the diketone **6** in 50.1% yield. The Wolff−Kischner reduction of the cyclophane diketone **6** gave **7** and an ether product **9**, but the separation of each product from the mixture was difficult. Therefore, compound **6** was reduced by the modified Clemmensen reduction procedure,[17] which gave **7** in 70.9% yield. Deprotection and dechlorination were simultaneously achieved by treating compound **7** with 10% Pd/C in the presence of ammonium formate. Cyclophane **1** was thus obtained in good yield from **7** (96.9%). The analogous reference compounds **2** and **3** were synthesized using the literature method reported by Osada et al.[18]

Crystallographic Analysis

Crystallographic analysis of **1** at low temperature (123 K) revealed that two kinds of molecules exist in the crystal. One of them has an O−H proton almost parallel to the benzene ring, which was observed in 80% probability. An O−H of another molecule is twisted and the proton is near the F atom. In Figure 2, these protons are shown in one molecule. The dihedral angles are ∠C(17)−C(18)−O(1)−H(19) = 1.7° and ∠C(17)−C(18)−O(1)−H(20) = 51.3°. The F···H(20) distance is 2.11 Å, which is much shorter than the sum of the van der Waals radii (2.67 Å) of the H atom (1.20 Å) and F atom (1.47 Å).[19] On the other hand, the F···H(19) distance is 2.90 Å and thus, H(19) apparently has no interaction with the F atom. The observed angles, ∠C(9)−F···H(20) = 105.5° and O−H(20)···F = 131.6°, and the F···H(20) distance are fairly near the values reported by Howard et al. and Caminati et al. The former found the potential minimum of the C(sp^2)−F···H−O hydrogen bond at 1.9 Å and the latter observed the angles and distances of ∠C−F···H−O = 93°, ∠O−H···F = 135° and r = 2.20 Å in the CH_2F_2−H_2O system. Furthermore, the O−H(20) distance is 0.99 Å, while O−H(19) is 0.82 Å. The two facts, formerly described as the short F···H(20) distance and the elongated O−H(20) bond, apparently indicate the existence of a hydrogen bond between H(20) and the F atom. However, the proportion of the hydrogen-bonded H atom is only 20%, and it is thus a weak interaction. According to the Boltzmann distribution law, the energy difference between O(19)−H and O(20)−H is only 1.6 kJ mol^{-1}, which can roughly be considered as the stabilization energy of the C−F···HO hydrogen bond of this system at 123 K.

Spectroscopic Investigations

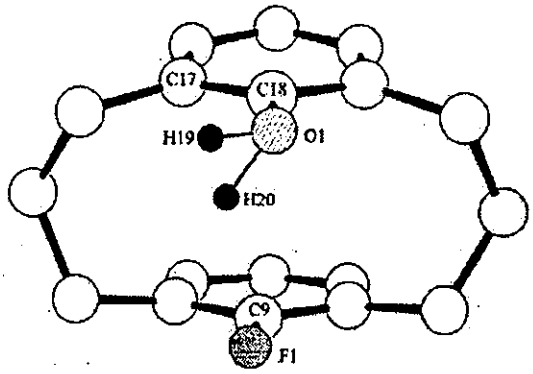

Figure 2. Molecular structure of the cyclophane 1

IR Spectra

In the IR spectra (Table 1), the ν_{OH} bands of **1** and **2** appeared as a sharp band around 3620 cm^{-1} in methylcyclohexane and CCl_4 at the concentration of 1.0×10^{-1} mol dm^{-3}. However, in diluted solution (10^{-2}, 10^{-3} and 10^{-4} mol dm^{-3}), no substantial changes were observed.

Table 1. IR spectra (ν_{OH} in cm^{-1}) of **1** and **2**: (A) crystal (transmittance IR), (B) KBr pellet, (C) in methylcyclohexane (1.0×10^{-4} mol dm^{-3}), and (D) in CCl_4 (1.0×10^{-4} mol dm^{-3})

	1	**2**
(A)	3610, 3560	3541, 3471
(B)	3610, 3560	3542, 3473
(C)	3620	3618
(D)	3621	3621

As seen in the crystallographic analysis, 20% of the OH proton binds to the F atom of **1**. Therefore, the IR spectra of the crystalline state are essential to detect the hydrogen bond. In the crystal lattice, the OH group is independent and no intermolecular interaction was observed (see Supporting Information; footnote on the first page of this article). Therefore, the band in the transmittance spectra of **1** should show the bands of the hydrogen-bond-free O–H and the C–F···H–O band. The transmittance IR spectra of the crystals of **1** and **2** were almost identical to those measured in KBr pellets. Both cyclophanes **1** and **2** have two ν_{OH} bands. In the case of **1**, a relatively broad band appears at 3560 cm^{-1} accompanied by a sharp band at 3610 cm^{-1}. Similarly, compound **2** has a relatively broad band at 3471 cm^{-1} and a sharp band at 3541 cm^{-1}. Unfortunately, crystallographic analysis of compound **2** failed, so the molecular arrangement and information about the hydrogen-bond pattern in the crystal are unknown.[20] Further discussion seems to be difficult because assignment of those ν_{OH} bands cannot be achieved. However, we can speculate that the C–F···H–O hydrogen bond may have anti-hydrogen-bond character because both bands of **1** are blue-shifted (70–90 cm^{-1}) compared to those of **2**.[21] The $\Delta\nu_{OH}$ is equivalent to the C–F···H–O hydrogen bond energy of 0.84–1.1 kJ·mol^{-1}.

NMR Spectra

Because the IR spectra in solution did not give any information, the ^1H and ^{19}F NMR spectra were evaluated. These results are summarized in Table 2. The chemical shifts of the phenolic OH protons of **1** and **2** in $CDCl_3$ at the concentrations of 1.0×10^{-1}, 1.0×10^{-2} and 1.0×10^{-3} mol·dm^{-3} were the same within the experimental errors [$\delta_{OH}(1)$ = 4.87 ppm; $\delta_{OH}(2)$ = 4.61 ppm]. On the other hand, the OH proton of **1** in [D_{14}]methylcyclohexane showed concentration-dependent chemical shifts, i.e., the OH proton signal appeared at δ = 4.75 ppm (1.0×10^{-1} mol·dm^{-3}), 4.62 ppm (1.0×10^{-2} mol·dm^{-3}), and 4.60 ppm (1.0×10^{-3} mol·dm^{-3}). In the case of cyclophane **2**, such chemical shifts were not observed at a concentration of 1.0×10^{-1} to 1.0×10^{-3} mol·dm^{-3}; it appears at δ = 4.20 ppm as a singlet. Although an interaction with $CDCl_3$ is apparent, the OH signal of **1** appears at a lower field than that of **2**, and this is the same in the noninteracting solvent, [D_{14}]methylcyclohexane. Therefore, the C–F···H–O hydrogen bond is obvious in the ^1H NMR spectra. Moreover, specific phenomena were seen in the spectrum of **1**, viz., the OH signal appeared as a doublet ($J_{H,F}$ = 6.0 Hz) which shows the through-space coupling with the fluorine atom. By irradiation of the F atom, the coupling disappeared and the doublet became a singlet. Furthermore, in a donating solvent such as [D_6]DMSO, the signal appeared as a singlet. This is further evidence of an O-H···F interaction.

The δ_F values of cyclophanes **1** and **3** were compared in their ^{19}F NMR spectra (Table 2). The differences were small, but in both $CDCl_3$ and [D_{14}]methylcyclohexane, chemical shifts of the F signal of cyclophane **1** are higher than those of **3** (1.0–1.6 ppm). This high-field shift of the F signal reminds us of similar phenomena in the metal complexes of fluorinated cage compounds.[22] The C–F···M^+ attractive interaction has now been unambiguously established by this group and Plenio et al.,[23,24] and the high-field shift of the F signal usually occurs during the C–F···M^+ interaction. Therefore, in the C–F···$H^{\delta+}$–$O^{\delta-}$ system, the same phenomena should also be observed. Here, again, the hydrogen bond is confirmed by comparison of the ^{19}F NMR spectra of cyclophanes **1** and **3**.

The temperature-dependent shift of the OH proton is another interesting feature in the study of the hydrogen bond. Variable-temperature ^1H NMR spectra of **1** and **2** were measured in nonpolar and polar solvents, [D_{14}]methylcyclohexane and [D_6]DMSO. As shown in Figure 3, the OH proton spectra of **1** and **2** are strongly temperature-dependent, especially below 240 K. In the case of **2**, two kinds of OH proton signals appeared below 243 K. At this temperature, conformational changes of the trimethylene bridge (boat ⇄ chair) are involved.[25] Therefore, the two OH protons correspond to those of the conformational isomers. In the case of cyclophane **1**, conformational changes also occur below 243 K. However, only one kind of OH proton

Table 2. NMR shifts of OH and F signals (1.0×10^{-2} mol·dm^{-3}) of the cyclophanes at 25 °C (A) in [D_{14}]methylcyclohexane, and (B) in $CDCl_3$

	^{1}H, δ(OH)		^{19}F, δ(^{19}F)	
	(A)	(B)	(A)	(B)
1	4.60 [d, J(H−F) = 6.6 Hz]	4.86 [d, J(H−F) = 6.0 Hz]	−120.3 (br. s)	−119.9 (br. s)
2	4.21 (s)	4.58 (br. s)	–	–
3	–	–	−118.7 (s)	−118.9 [d, J(H−F) = 3.5 Hz]

was observed. In the polar solvent ([D_6]DMSO), the OH signal of **1** is shifted to a high-field region compared to that of **2** (Δδ = −0.25 ppm at 298 K). This phenomenon reflects that the hydrogen bond between **1** and DMSO is inhibited by the intramolecular hydrogen bond.

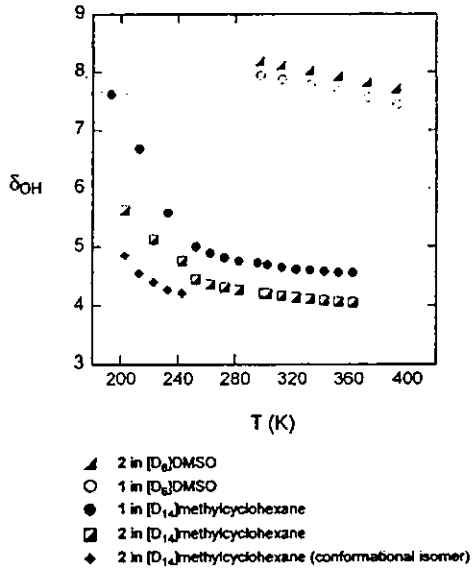

Figure 3. Plots of δ_{OH} in [D_6]DMSO and [D_{14}]methylcyclohexane at various temperatures

The difference of chemical shift of the OH proton, Δδ, between **1** and **2** is almost constant (Δδ ≈ 0.5 ppm in [D_{14}]methylcyclohexane) between 273 and 363 K, and the Δδ value indicates the C-F···H−O binding energy. Schaefer represented the relationship between hydrogen-bond energy and chemical shift of *ortho*-substituted phenols.[26] The empirical equation $\Delta\delta_{OH} = -0.4 + E$ (E is the hydrogen-bond energy in kcal·mol^{-1}) can be applied to our cyclophane system. According to the equation, the C-F···H−O hydrogen bond of **1** is estimated to be 0.89 kcal·mol^{-1} (3.7 kJ mol^{-1}) in [D_{14}]methylcyclohexaneand 0.65 kcal·mol^{-1} (2.7 kJ·mol^{-1}) in [D_6]DMSO at 298 K.

From the results of the crystallographic analysis, IR spectra and NMR spectra, we estimated the C-F···H−O hydrogen bond energy of **1** to be 0.84−1.6 kJ·mol^{-1} in the solid state and 2.7−3.7 kJ·mol^{-1} in solution.

Conclusion

A [3.3]metacyclophane, which is composed of a phenol unit and a fluorobenzene unit, was synthesized. It is a simple model for the investigation of the C−F···H−O hydrogen bond. The cyclophane skeleton is suitable for realizing the ideal F···H−O distance and angles, and to obtain the entropy. Actually, evidence for the C−F···H−O hydrogen bond is observed from the results of the crystallographic analysis. Two kinds of OH hydrogen atoms are observed and one of them is pointing towards the fluorine atom. The H···F distance is shorter than the sum of the van der Waals radii of the H and F atoms, and the O−H bond is longer than that of another proton which is separated from the F atom. In the ^{1}H NMR spectrum, the OH proton signal of **1** appears at a lower field than that of the fluorine-free analog **2**. Furthermore, through-space coupling between the F atom and OH proton is observed. Although the IR spectra did not give a clear result, it is speculated that the C−F···H−O hydrogen bond has an anti-hydrogen-bond character. The C−F···H−O hydrogen bond energy in this system was estimated to be 0.84−3.7 kJ·mol^{-1} according to the results of the crystallographic analysis and the IR and NMR spectra. Although the C−F···H−O hydrogen bond is very rare in the crystallographic database, it is possible to observe it by this simple molecular design. A forcibly approached OH and CF unit with the appropriate distance and angle clarified this weak interaction.

Experimental Section

General Procedure: Melting points (uncorrected): Yanaco MP-500D apparatus in Ar sealed tubes. NMR: Bruker DPX-400 (400.1 MHz for ^{1}H, 100.6 MHz for ^{13}C, and 376.5 MHz for ^{19}F with TMS and $CFCl_3$ as internal references, respectively) and JEOL GSX 270 (270 MHz for ^{1}H and 67.9 MHz for ^{13}C). IR: JASCO IR-700 [methylcyclohexane in NaCl cells (0.1 and 0.5 mm) at 25°C]. FAB and EI MS: JEOL JMS-SX/SX102A. Elemental analysis: the Service Centre of the Elementary Analysis of Organic Compounds affiliated with the Faculty of Science, Kyushu University.

Crystallographic Data of 1: $C_{18}H_{19}OF$, M_r = 270.35 g·mol^{-1}, platelet crystal (grown from *n*-hexane), size 0.40 × 0.20 × 0.05 mm, monoclinic, space group $P2_1$ (no. 4), a = 8.719(1) Å, b = 8.552(1) Å, c = 9.599(1) Å, V = 695.3(2) Å^3, Z = 2, $\rho_{calcd.}$ = 1.291 g·cm^{-3}, μ(Cu-K$_\alpha$) = 7.01 cm^{-1}, F(000) = 288.00, T = −150 ± 1 °C using the ω-2θ scan technique to a maximum 2θ value of 136.4°. A total

of 4177 reflections were collected. The final cycle of the full-matrix least-squares refinement was based on 1990 observed reflections [$I > 2\sigma(I)$] and 182 variable parameters and converged with unweighted and weighted agreement factors of $R = 0.067$, $Rw = 0.202$, and GOF = 1.09. The maximum and minimum peaks on the final difference Fourier map corresponded to 0.22 and −0.25 $e^- \cdot Å^{-3}$, respectively. The ratio of two kinds of molecules in the crystal was calculated and the probability of 0.8:0.2 afforded the optimal result. CCDC-213846 contains the supplementary crystallographic data for this paper. These data can be obtained free of charge at www.ccdc.cam.ac.uk/conts/retrieving.html [or from the Cambridge Crystallographic Data Centre, 12 Union Road, Cambridge CB2 1EZ, UK; Fax: (internat.) + 44-1223/336-033; E-mail: deposit@ccdc.cam.ac.uk].

1-Benzyloxy-4-chloro-2,6-bis(hydroxymethyl)benzene: The compound was prepared by the reaction between 4-chloro-2,6-bis(hydroxymethyl)phenol and benzyl bromide with K_2CO_3 as a base in acetone (86.4%). Recrystallization from toluene/methanol gave a colorless powder; m.p. 125.2−126.9 °C. ^{1}H NMR ([D$_6$]DMSO): δ = 7.46−7.35 (m, 5 H, ArH), 7.33 (s, 2 H, ArH), 5.27 (t, $^3J_{H,H}$ = 5.5 Hz, 2 H, OH), 4.83 (s, 2 H, CH_2), 4.52 (d, $^3J_{H,H}$ = 6.0 Hz, 4 H, CH_2) ppm. FAB-MS: *m/z* = 278.1, 280.1. $C_{15}H_{15}ClO_3$ (278.73): calcd. C 64.64, H 5.42; found C 64.72; H 5.46.

1-Benzyloxy-2,6-bis(bromomethyl)-4-chlorobenzene (4a): The compound was prepared by treatment of 1-benzyloxy-4-chloro-2,6-bis(hydroxymethyl)benzene with PBr_3 in diethyl ether (yield 86.8%). The resultant powder was recrystallized from *n*-hexane. Colorless solid, m.p. 97.3−98.5 °C. ^{1}H NMR ($CDCl_3$): δ = 7.53−7.39 (m, 5 H, ArH), 7.38 (s, 2 H, ArH), 5.16 (s, 2 H, CH_2), 4.46 (s, 4 H, CH_2) ppm. FAB-MS: *m/z* = 402.9, 403.9, 404.9 [M + H$^+$]. $C_{15}H_{13}Br_2ClO \cdot 1/12C_6H_{14}$ (411.71): calcd. C 45.22, H 3.47; found C 45.08; H 3.30.

1-Fluoro-2,6-bis[2-isocyano-2-(4-tolylsulfonyl)ethyl]benzene (5): The compound was synthesized by reaction between 2,6-bis(bromomethyl)-1-fluorobenzene and TosMIC (yield 62.8%) according to the literature method.[16] Recrystallization from CH_2Cl_2/diethyl ether gave colorless fine crystals, m.p. 112 °C (dec.). ^{1}H NMR ($CDCl_3$): δ = 7.91, 7.45 (AB q, $^3J_{H,H}$ = 8.4 Hz, 8 H, ArH), 7.28−7.13 (m, 3 H, ArH), 4.68 (dd, $^3J_{H,H}$ = 10.8 Hz, 2 H, CH), 3.73−3.04 (m, 4 H, CH_2), 2.50 (s, 6 H, CH_3) ppm. FAB-MS: no molecular peak was found. $C_{26}H_{23}FN_2S_2O_4$ (510.60): calcd. C 61.16, H 4.54, N 5.49; found C 60.88, H 4.63; N 5.52.

9-Benzyloxy-6-chloro-18-fluoro[3.3]metacyclophane-2,11-dione (6): A mixture of CH_2Cl_2 (1.3 L), 40% aq. NaOH (50 mL), and nBu$_4$NI (1.69 g, 4.58 mmol) was heated under reflux with vigorous stirring. To this mixture, a solution of **4a** (4.05 g, 10.0 mmol) and **5** (5.62 g, 11.0 mmol) in CH_2Cl_2 (250 mL) was added dropwise over a period of 6 h. Additional heating and stirring were continued for 5 h. After cooling, the organic phase was separated and washed with brine. The solution was concentrated to ca. 300 mL, conc. HCl (30 mL) was added and the mixture was stirred at room temperature for 40 min. The organic phase was separated, washed with water and dried with $MgSO_4$. The solvent was removed under reduced pressure and a small amount of acetone was added. After several hours, the precipitated colorless prisms were collected (yield 2.12 g, 50.1%), m.p. 138.4−138.8 °C. ^{1}H NMR ($CDCl_3$): δ = 7.53−7.32 (m, 3 H, ArH), 7.24 (s, 2 H, ArH), 7.12 (dd, $^3J_{H,H}$ = 7.0 Hz, 2 H, ArH), 7.05−7.03 (m, 2 H, ArH), 6.84 (t, $^3J_{H,H}$ = 7.5 Hz, 1 H, ArH), 4.32 (s, 2 H, CH_2), 3.80−3.15 (m, 8 H, CH_2) ppm. FAB-MS: *m/z* = 423 [M + H$^+$]. $C_{25}H_{20}ClFO_3$ (422.88): calcd. C 71.01, H 4.77; found C 71.03; H 4.78.

9-Benzyloxy-6-chloro-18-fluoro[3.3]metacyclophane (7): Dry HCl gas was bubbled into dry ether (80 mL) at −10 °C for 1 h, and compound **6** (1.48 g, 3.5 mmol) was added. The resultant suspension was cooled to −20 °C and activated Zn powder (2.0 g) was added in small portions. After the addition, the temperature was raised to −5 °C and the mixture stirred for 2 h. The resultant mixture was poured onto crushed ice (40 g) and the organic phase was separated. The aqueous phase was extracted twice with ether, and all the diethyl ether solutions were combined. They were washed with aq. $NaHCO_3$ and dried with $MgSO_4$, the solvent was removed and the resultant powder was recrystallized from *n*-hexane. Colorless prisms (yield 980 mg, 70.9%), m.p. 102.1−102.6 °C. ^{1}H NMR ($CDCl_3$): δ = 7.53−7.31 (m, 5 H, ArH), 6.73 (m, 1 H, ArH), 6.63 (dd, $^3J_{H,H}$ = 7.0 Hz, 2 H, ArH), 6.52 (s, 2 H, ArH), 4.65 (s, 2 H, CH_2), 3.10−3.02 (m, 4 H, CH_2), 2.52−2.33 (m, 6 H, CH_2), 1.85−1.75 (m, 2 H, CH_2) ppm. FAB-MS: *m/z* = 394 [M$^+$]. $C_{25}H_{24}ClFO$ (394.91): calcd. C 76.03, H 6.13; found C 75.99, H 6.10.

18-Fluoro-9-hydroxy[3.3]metacyclophane (1): A mixture of the cyclophane **7** (197 mg, 0.50 mmol) and ammonium formate (221 mg, 3.5 mmol) in MeOH (60 mL) was stirred at room temperature under N_2; 10% Pd/C (100 mg) was added to the mixture, which was then stirred at room temperature for 5 h. The mixture was filtered through Celite and the solvent was removed. The resultant mixture was extracted with diethyl ether and the solution was washed with brine and dried with $MgSO_4$. After removal of the solvent, compound **1a** was obtained as a white powder, which was recrystallized from *n*-hexane. Colorless prisms (yield 131 mg, 96.9%), m.p. 84.5−84.8 °C. ^{1}H NMR ($CDCl_3$): δ = 6.63−6.53 (m, 5 H, ArH), 6.39 (t, $^3J_{H,H}$ = 7.0 Hz, 1 H, ArH), 4.87 (d, $^3J_{H,H}$ = 6.0 Hz, 1 H, CH_2), 3.09−2.99 (m, 4 H, CH_2), 2.65−2.54 (m, 4 H, CH_2), 2.42−2.35 (m, 2 H, CH_2), 1.92−1.81(m, 2 H, CH_2) ppm. FAB-MS: *m/z* = 270 [M$^+$]. $C_{18}H_{19}FO$ (270.34): calcd. C 79.97, H 7.08; found C 79.91, H 7.08.

1-Acetoxy-2,6-bis(bromomethyl)-4-chlorobenzene (4b): A mixture of 2,6-bis(bromomethyl)-4-chlorophenol (6.29 g, 20 mmol), acetic anhydride (2.4 mL, 25 mmol), and $BF_3 \cdot Et_2O$ (0.1 mL, 0.8 mmol) in dry diethyl ether (20 mL) was stirred at room temperature for 10 h. The mixture was added to water (20 mL) and the resultant white powder was collected by filtration and washed with water to give the pure compound (yield 6.10 g, 85.6%). Recrystallization from *n*-hexane gave colorless needles, m.p. 143.3−144.2 °C. ^{1}H NMR ($CDCl_3$): δ = 7.39 (s, 2 H, ArH), 4.31(s, 4 H, CH_2), 2.15 (s, 3 H, CH_3) ppm. FAB-MS: *m/z* = 354.9, 356.9, 358.9 [M + H$^+$]. $C_{10}H_9Br_2ClO_2$ (356.44): calcd. C 33.70, H 2.55; found C 33.80, H 2.50.

Compound 8: A solution of **4b** (3.56 g, 10 mmol) and **5** (5.11 g, 10 mmol) in dry DMF (500 mL) was added to a stirred mixture of NaH (60% in mineral oil, 1.20 g, 30 mmol) and dry DMF (700 mL) at room temperature over a period of 10 h. Additional stirring was continued for 10 h and then the mixture was quenched with MeOH. The solvent was removed under reduced pressure and MeOH was added. After several hours, pale-yellow crystals precipitated. The crystals were collected by filtration and dissolved in CH_2Cl_2 (300 mL). Concentrated HCl (20 mL) was added to the solution, which was stirred at room temperature for 30 min. The organic phase was separated, washed with water and dried with $MgSO_4$. The solvent was removed and a small amount of acetone was added to the residue. Colorless prisms that precipitated after several hours were collected (yield 1.10 g, 35.2%), m.p. 259.7−260.1 °C. ^{1}H NMR ($CDCl_3$): δ = 7.17−7.13 (m, 5 H, ArH), 3.72−3.56

(m, 8 H, CH_2) ppm. FAB-MS: *m/z* = 313 [M + H^+]. $C_{18}H_{13}ClO_3$ (312.75): calcd. C 69.13, H 4.19; found C 69.15, H 4.20.

Compound 9: A mixture of **8** (665 mg, 2.13 mmol), 80% hydrazine hydrate (3.4 mL, 53 mmol), diethylene glycol (30 mL), and KOH (1.57 g, 23.8 mmol) was heated at 120 °C for 2 h, and then the temperature was raised to 180 °C. The water generated during the reaction was removed by a Dean–Stark condenser. Additional heating was continued for 2 h, then the mixture was cooled, poured into water and extracted twice with CH_2Cl_2. The organic phase was washed with water and brine, then dried with $MgSO_4$. The solvent was removed and the residue was recrystallized from MeOH. Colorless needles (421 mg, 69.4%). M.p. 112.3–112.7 °C. ^1H NMR ($CDCl_3$): δ = 6.97–6.89 (m, 5 H, ArH), 3.21–3.13 (m, 2 H, CH_2), 2.81–2.70 (m, 2 H, CH_2), 2.39–2.32 (m, 1 H, CH_2), 1.76–1.55 (m, 1 H, CH_2) ppm. FAB-MS: *m/z* = 284 [M^+]. $C_{18}H_{17}ClO$ (284.78): calcd. C 75.92, H 6.02; found C 75.84, H 6.05.

[1] P. Murray-Rust, W. C. Stallings, C. T. Monti, R. K. Prestone, J. P. Glusker, *J. Am. Chem. Soc.* **1983**, *105*, 3206–3214.
[2] J. D. Dunitz, R. Taylor, *Chem. Eur. J.* **1997**, *3*, 89–98.
[3] L. Shimoni, J. P. Glusker, *Struct. Chem.* **1994**, *5*, 383–397.
[4] S. J. Borwick, J. A. K. Howard, C. W. Lehmann, D. O'Hagan, *Acta Crystallogr., Sect. C* **1997**, *53*, 124–126.
[5] T. J. Barbarich, C. D. Rithner, S. M. Miller, O. P. Anderson, S. H. Strauss, *J. Am. Chem. Soc.* **1999**, *121*, 4280–4281.
[6] M. Pham, M. Gdaniec, T. Polonski, *J. Org. Chem.* **1998**, *63*, 3731–3734.
[7] N. Shibata, B. K. Das, K. Harada, Y. Takeuchi, M. Bando, *Synlett* **2001**, 1755–1758.
[8] K.-M. Marstokk, H. MØllendal, *Acta Chem. Scand.* **1999**, *53*, 202–208.
[9] A. Fujii, A. Iwasaki, N. Mikami, *Chem. Lett.* **1997**, 1099–1100.
[10] A. Kovács, I. Mascsári, I. Hargittai, *J. Phys. Chem. A* **1999**, *113*, 3110–3114.
[11] A. D. Headley, S. D. Starnes, *J. Comput. Chem.* **2000**, *21*, 426–431.
[12] J. E. Monat, R. R. Toczyowski, S. M. Cybulski, *J. Phys. Chem. A* **2001**, *105*, 9004–9013.
[13] J. A. K. Howard, V. J. Hoy, D. O'Hagan, G. T. Smith, *Tetrahedron* **1996**, *52*, 12613–12622.
[14] W. Caminati, S. Melandri, I. Rossi, P. G. Favero, *J. Am. Chem. Soc.* **1999**, *121*, 10098–10101.
[15] H. Takemura, S. Nakashima, N. Kon, M. Yasutake, T. Shinmyozu, T. Inazu, *J. Am. Chem. Soc.* **2001**, *123*, 9293–9298.
[16] [16a] K. Kurosawa, M. Suenaga, T. Inazu, T. Yoshino, *Tetrahedron Lett.* **1982**, *23*, 5335–5338. [16b] T. Shinmyozu, Y. Hirai, T. Inazu, *J. Org. Chem.* **1986**, *51*, 1551–1555.
[17] S. Yamamura, M. Toda, Y. Hirata, *Org. Synth. Coll. Vol.* **1988**, *6*, 289–292.
[18] [18a] S. Osada, M. Suenaga, Y. Miyahara, T. Shinmyozu, T. Inazu, *Mem. Fac. Sci., Kyushu Univ., Ser. C* **1993**, *19*, 33–38. [18b] S. Osada, Y. Miyahara, N. Shimizu, T. Inazu, *Chem. Lett.* **1995**, 1103–1104. [18c] S. Osada, Thesis, Kyushu University, 1995.
[19] A. Bondi, *J. Phys. Chem.* **1964**, *68*, 441–451.
[20] Crystallographic analysis of *p*-Cl analog of **2** (6-chloro-9-hydroxy[3.3]metacyclophane) succeeded. It showed intermolecular O–H···O hydrogen bonds and even intermolecular Cl···H–O hydrogen bonds. Unpublished results.
[21] [21a] P. Hobza, V. Spirko, H. L. Selzle, E. W. Schlag, *J. Phys. Chem. A* **1998**, *102*, 2501–2504. [21b] E. Cubero, M. Orozco, P. Hobza, F. J. Luque, *J. Phys. Chem. A* **1999**, *103*, 6394–6401. [21c] E. Cubero, M. Orozco, F. J. Luque, *Chem. Phys. Lett.* **1999**, *310*, 445–450. [21d] P. Hobza, Z. Havlas, *Chem. Phys. Lett.* **1999**, *303*, 447–452. [21e] P. Hobza, Z. Havlas, *Chem. Rev.* **2000**, *100*, 4253–4264. [21f] B. J. van der Veken, W. A. Herrebout, R. Szostak, D. N. Shchepkin, Z. Havlas, P. Hobza, *J. Am. Chem. Soc.* **2001**, *123*, 12290–12293.
[22] [22a] H. Takemura, H. Kariyazono, M. Yasutake, N. Kon, K. Tani, K. Sako, T. Shinmyozu, T. Inazu, *Eur. J. Org. Chem.* **2000**, 141–148. [22b] H. Takemura, S. Nakashima, N. Kon, T. Inazu, *Tetrahedron Lett.* **2000**, *41*, 6105–6109. [22c] H. Takemura, *J. Syn. Org. Chem. Jpn.* **2002**, *60*, 963–973.
[23] [23a] H. Takemura, N. Kon, M. Yasutake, H. Kariyazono, T. Shinmyozu, T. Inazu, *Angew. Chem.* **1999**, *111*, 1012–1014; *Angew. Chem. Int. Ed.* **1999**, *38*, 959–961. [23b] H. Takemura, N. Kon, M. Yasutake, S. Nakashima, T. Shinmyozu, T. Inazu, *Chem. Eur. J.* **2000**, *6*, 2334–2337. [23c] H. Takemura, N. Kon, M. Kotoku, S. Nakashima, K. Otsuka, M. Yasutake, T. Shinmyozu, T. Inazu, *J. Org. Chem.* **2001**, *66*, 2778–2783. [23d] H. Takemura, S. Nakashima, N. Kon, M. Yasutake, T. Shinmyozu, T. Inazu, *J. Am. Chem. Soc.* **2001**, *123*, 9293–9298. [23e] H. Takemura, in *Cyclophane Chemistry for the 21st Century* (Ed.: H. Takemura), Transworld Research Network, India, **2003**, p. 127–148.
[24] [24a] H. Plenio, R. Diodone, *Angew. Chem.* **1994**, *106*, 2267–2269; *Angew. Chem. Int. Ed. Engl.* **1994**, *33*, 2175–2177. [24b] H. Plenio, D. Burth, *J. Chem. Soc., Chem. Commun.* **1994**, 2297–2298. [24c] H. Plenio, R. Diodone, *J. Am. Chem. Soc.* **1996**, *118*, 356–367. [24d] H. Plenio, R. Diodone, *Chem. Ber.* **1996**, *129*, 1211–1217. [24e] H. Plenio, R. Diodone, *Chem. Ber./Recueil* **1997**, *130*, 963–968. [24f] H. Plenio, J. Hermann, R. Diodone, *Inorg. Chem.* **1997**, *36*, 5722–5729. [24g] H. Plenio, R. Diodone, D. Badura, *Angew. Chem.* **1997**, *109*, 130–132; *Angew. Chem. Int. Ed. Engl.* **1997**, *36*, 156–158. [24h] H. Plenio, *Chem. Rev.* **1997**, *97*, 3363–3384, and references cited therein.
[25] [25a] H. Takemura, H. Kariyazono, N. Kon, T. Shinmyozu, T. Inazu, *J. Org. Chem.* **1999**, *64*, 9077–9079.. [25b] K. Sako, T. Hirakawa, N. Fujimoto, T. Shinmyozu, T. Inazu, H. Horimoto, *Tetrahedron Lett.* **1988**, *29*, 6275–6278. [25c] K. Sako, T. Shinmyozu, H. Takemura, M. Suenaga, T. Inazu, *J. Org. Chem.* **1992**, *57*, 6536–6541. [25d] M. F. Semmelhack, J. J. Harrison, D. C. Young, A. Gutiérrez, S. Rafii, J. Clardy, *J. Am. Chem. Soc.* **1985**, *107*, 7508–7514.
[26] T. Schaefer, *J. Phys. Chem.* **1975**, *79*, 1888–1890.

Received November 1, 2003

Available online at www.sciencedirect.com
SCIENCE DIRECT®
Biomaterials 26 (2005) 3929–3939
Biomaterials
www.elsevier.com/locate/biomaterials

Electrospun nano- to microfiber fabrics made of biodegradable copolyesters: structural characteristics, mechanical properties and cell adhesion potential

Il Keun Kwon, Satoru Kidoaki, Takehisa Matsuda*

Department of Biomedical Engineering, Graduate School of Medicines, Kyushu University, 3-1-1 Maidashi, Higashiku, Fukuoka city, Fukuoka 812-8582, Japan

Received 20 May 2004; accepted 14 October 2004

Abstract

Nano- to micro-structured biodegradable poly(L-lactide-*co*-ε-caprolactone) (PLCL) fabrics were prepared by electrospinning. Electrospun microfiber fabrics with different compositions of PLCL (mol% in feed; 70/30, 50/50, and 30/70), poly(L-lactide) (PLL) and poly(ε-caprolactone) (PCL) were obtained using methylene chloride (MC) as a solvent. The PLL microfiber exhibited a nanoscale-pore structure with a pore diameter of approximately 200–800 nm at the surface and subsurface regions, whereas such a surface structure was hardly observed in other polymers containing CL. The microfiber fabric made of PLCL 50/50 was elastomeric. Nanoscale-fiber fabrics with PLCL 50/50 (approx. 0.3 or 1.2 μm in diameter) were electrospun using 1,1,1,3,3,3-hexafluoro-2-propanol (HFIP) as a solvent. Mercury porosimetry showed that the decrease in the fiber diameter of the fabric decreased porosity, but increased fiber density and mechanical strength. Human umbilical vein endothelial cells (HUVECs) were adhered well and proliferated on the small-diameter-fiber fabrics (0.3 and 1.2 μm in diameter), both of which are dense fabrics, whereas markedly reduced cell adhesion, restricted cell spreading and no signs of proliferation were observed on the large-diameter-fiber fabric (7.0 μm in diameter). The potential biomedical application of electrospun PLCL 50/50 was discussed.

Keywords: Electrospinning; Nanofibers; Microfibers; Dielectric constant; Human umbilical vein endothelial cell (HUVEC)

1. Introduction

Various micropored polymeric scaffold fabrication techniques of generating interconnected pores on a few tenths to several hundreds of micrometer scale, which include fiber bonding [1], solid free-form fabrication [2], and salt extraction [3], have been widely used in tissue engineering. Recent studies showed that cells recognize nanometric topologies of fibrous or microporous structure. Such a nanoscale structure geometrically or topologically mimics the native state of extracellular matrix (ECM) biomacromolecules in living tissues, such as collagen, hyaluronic acid, laminin, and fibronectin and their complex supramolecular assemblies [4,5]. The fabrication and design of submicron- to nanoscale structural architectures have received much attention in medical applications [6–10].

Electrospinning is a fiber spinning technique driven by a high-voltage electrostatic field using a polymeric solution or liquid that produces polymer fibers with diameters ranging from several micrometers down to 100 nm or less [11,12]. The variables controlling the behavior of the electrified fluid jet during electrospinning can be divided into fluid properties and operating parameters. The relevant fluid properties are viscosity (η), conductivity (K), dielectric constant (ε), boiling point (bp), and surface tension (γ). The operating parameters are flow rate (Q), applied electric potential

*Corresponding author. Tel.: +81 92 642 6210; fax: +81 92 642 6212.
E-mail address: matsuda@med.kyushu-u.ac.jp (T. Matsuda).

0142-9612/$ - see front matter © 2004 Elsevier Ltd. All rights reserved.
doi:10.1016/j.biomaterials.2004.10.007

(V), and the distance between the tip and the collector called air gap (d) [11,12].

In the design of a provisional scaffolding material for the fabrication of engineered tissues, a candidate polymer should possess appropriate mechanical properties, which are suitable for target applications, and its degradation products during implantation should be metabolic substances produced by the living body, thus guaranteeing inherent nontoxicity. Over the past years, hydrolyzable and biocompatible copolymers of ε-caprolactone (CL) and L-lactide (LL) have been of great interest for medical applications [13,14]. Polylactide (PLL) is a crystallizable hard and brittle material, whereas poly(ε-caprolactone) (PCL) is a semicrystalline material with rubbery properties [3,15]. Copolymers of LL and CL (PLCL) exhibit various mechanical properties, depending on their composition [16]. For example, the high-molecular-weight equimolar copolymer PLCL 50/50 is a biodegradable elastomer [17].

In this study, a series of high-molecular-weight PLCLs of different compositions was prepared by ring-opening copolymerization. As a continuation of our series of studies on electrospinning technology in biomedical application, the followings were studied in this article: (1) The copolymer composition dependency on the physical state and mechanical properties of electrospun fibers. (2) Internal structural features including and mechanical integrity of electrospun fabrics made of the equimolar copolymer, which were prepared using different solvents under different operation conditions, were evaluated in terms of their fiber diameter, and porosity, and (3) the dependency of cell adhesion and proliferation potentials on surface fiber density.

2. Materials and methods

2.1. Materials

All the solvents and reagents used were purchased from either Wako Pure Chemical Industries Ltd. (Osaka, Japan) or Sigma-Aldrich Japan, Inc. (Tokyo, Japan). L-lactide (LL) was recrystallized from ethyl acetate. ε-caprolactone (CL) was purified by drying over calcium hydride (CaH_2) for 24 h at room temperature and then distilled it under a reduced pressure (approximately 0.3 mmHg) at 55 °C. Stannous octoate ($Sn(Oct)_2$) was purified by vacuum distillation at 175 °C (ca. 0.2 mmHg). Toluene was thoroughly dried by distillation over CaH_2. The other solvents and reagents were of extra pure grade and used as received.

2.2. Copolymerization

The equimolar copolymerization of PLCL was carried out in a 50-mL glass ampoule containing 14.4 g (0.1 mol) of LL and 11.4 g (0.1 mol) of CL. 0.005 g (1.3×10^{-5} mol) of $Sn(Oct)_2$ diluted with dried toluene was added to the ampoule using a syringe. The ampoule was heated under a reduced pressure to remove toluene, and then sealed by heating with a torch under vacuum. The copolymerization was carried at 150 °C in a silicone oil bath for 24 h. The copolymer was obtained by precipitation in methanol and vacuum-dried for 48 h at room temperature. Irrespective of the composition of PLCL, the yield was found to be almost 100%. The process conditions used for the other feed ratios of LL to CL (100/0, 70/30, 30/70, and 0/100 mol/mol) were the same as those used for PLCL 50/50.

2.3. PLCL copolymer characterizations

Copolymer compositions were calculated from ^{1}H-NMR spectra, which were recorded on JNM-AL300 (JEOL, Tokyo, Japan). Chemical shifts are given in δ from Me_4Si as an internal standard. The number-average molecular weight (Mn) of each polymer was determined using a gel permeation chromatograph (GPC) (Waters 410, Milford, MA) fitted with microstyragel columns and calibrated with narrow polystyrene standards (Aldrich). Chloroform was used as the mobile phase at a flow rate of 1.0 ml/min at 30 °C.

2.4. Electrospinning apparatus

The setup of our electrospinning apparatus was reported in our previous work [18]. Briefly, it consisted of a high-voltage-power supply (HSP-30k-2; Nippon Stabilizer Inc., Osaka, Japan), an infusion pump (model 22; Harvard Apparatus Inc., Holliston, MA), a glass syringe equipped with a stainless-steel blunt-ended needle [outer diameter, 1.0 mm; inner diameter, 0.8 mm], and an aluminum plate-type collector.

2.5. Electrospinning

For the electrospun microfiber fabrics, a series of PLCL solutions was prepared by dissolving the copolymers in methylene chloride (MC) at a concentration of 4–11 wt%, depending on the composition of copolymer. The polymer solution was delivered at a constant flow rate (10 ml/h) using an infusion pump to the stainless-steel blunt-ended needle with an air gap between the metal collector and the needle tip of 30 cm at a driving voltage of 12.5 kV (Table 2). For the electrospun submicron or nanofiber fabrics with PLCL 50/50, the conditions were as follows: solvent, 1,1,1,3,3,3-hexafluoro-2-propanol (HFIP, Sigma Chemical Co., St. Louis, MO); polymer concentration, 3 wt%; flow rate, 5 or 10 ml/h; air gap, 20 cm; and driving voltage, 15 or 30 kV (Table 3).

2.6. Scanning electron microscopy

The electrospun products of PLCL were sputter-coated with platinum, and the microscopic structure was observed by scanning electron microscopy (SEM, JSM-840A, JEOL Ltd., Tokyo, Japan) at an acceleration voltage of 8 kV. The mean fiber diameters of the electrospun PLCL fabrics were calculated using 20 fibers seen on each SEM image.

2.7. Porosimetry

Pore diameter distribution, total pore volume, and the porosity of the electrospun PLCL 50/50 nano- to microfiber fabrics (approx. 140 μm thickness) were measured using a mercury intrusion porosimeter (Poresizer 9320, Micromeritics Instrument Co., Norcross, GA) in mercury intrusion under an increasing pressure from 100 kPa to 207 MPa, which was carried out at Toray Research Center (Tokyo, Japan). The determination of porosity was based on the relationship between the applied pressure and the pore diameter into which mercury intrudes, according to the Washburn equation:

$$D = (-4\gamma \cos\theta)/P$$

where P is the applied pressure, D is the pore diameter, γ is the surface tension of the mercury (484 mN m^{-1}) and θ is the contact angle between mercury and the pore wall, taken as 141.3° [19].

2.8. Tensile test

The uniaxial tensile properties of the electrospun PLCL nano- to microfiber fabrics (5 × 20 × 0.14 mm) were determined using a tensile tester (Rheoner II, Yamaden Co. Ltd., Tokyo, Japan). The stress–strain curves of the samples were obtained from the load-deformation curves recorded at a stretching speed of 0.5 mm/s.

2.9. Cell culture examination

The electrospun fabrics (10 × 10 mm^2), sterilized with 70% ethanol, followed by washing with phosphate buffered saline (PBS) and subsequent air-drying, were placed on the bottom of a 24-well culture dish (Corning, NY). Human umbilical vein endothelial cells (HUVECs, obtained from the American Type Culture Collection, 5 × 10^4 cells/cm^2) were seeded and cultured in the dish in an endothelial cell basal medium 2 (EC-2, Clonetics, Walkersville, MD) supplemented with 5% fetal bovine serum (FBS, Life Technologies, Rockville, MD) and 0.94% microvascular endothelial cell medium-2 (EGM-2 MV, Clonetics), which contained a human endothelial growth factor, a human fibroblast growth factor, a human epidermal growth factor, insulin-like growth factor I, ascorbic acid, and hydrocortisone acetate, at 37 °C in a humidified 5% CO_2 atmosphere. The number of cells on the electrospun fabrics was determined using a hematocytometer after detaching the cells from the fabrics using 0.1%-trypsin (Life Technologies).

2.10. Statistical analysis

All the quantitative values were expressed as a mean ± standard deviation. Statistical analysis was carried out using an ANOVA with a Scheffé test post hoc ($p<0.05$) using Statview for Windows (SAS Institute Inc., Copyright 1992–1998) version 5.0.

3. Results

3.1. Electrospun PLCL microfiber fabrics

A series of PLCL copolymers with different copolymer composition was synthesized by ring-opening (co)polymerization in the presence of $Sn(Oct)_2$ in bulk at 150 °C (Scheme 1). Table 1 summarizes the reaction conditions, feed monomer compositions, copolymer compositions, molecular weights and the polydispersities of their copolymers. Irrespective of the type of (co)polymer, the yield was approximately 92–97%. The compositions of the copolymers were determined by ^{1}H-NMR spectroscopy (Fig. 1). The methine protons of the lactide unit appeared at δ 5.1–5.2 (Fig. 1a, a′), which can be ascribed to the sequence distribution of the lactyl and caproyl units. The methylene protons of the caproyl unit adjacent to the ester group appeared at δ 4.0–4.2 (Fig. 1c, c′) and δ 2.3–2.5 (Fig. 1g, g′). The copolymer compositions determined from these relative intensities were almost identical to those of the initial feed compositions, as expected from the fact that the reaction was completed at almost full conversion. The

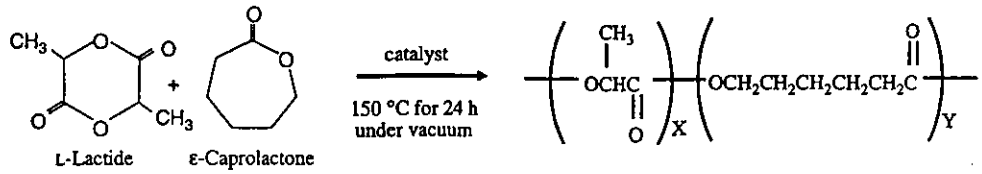

L-Lactide ε-Caprolactone

Scheme 1. Schematics of preparation of poly(L-lactide-*co*-ε-caprolactone) (PLCL).

Table 1
Biodegradable poly(L-lactide-*co*-ε-caprolactone) (PLCL) copolymer[a]

Polymer code	Monomer feed ratio	Copolymer composition[b]	Molecular weight[c]		Physical state at 25 °C
	LL:CL	LL:CL	Mn	Mw/Mn	
PLL	100:0	100:0	4.5×10^5	1.3	Hard solid
PLCL 70/30	70:30	74:26	2.0×10^5	1.8	Hard solid
PLCL 50/50	50:50	50:50	2.6×10^5	1.8	Elastomer
PLCL 30/70	30:70	31:69	1.5×10^5	2.2	Gummy solid
PCL	0:100	0:100	1.8×10^5	2.1	Hard solid

[a]Reaction condition; 150 °C for 24 h under vacuum.
[b]Determined by ^{1}H-NMR.
[c]Determined by GPC in chloroform (Polystyrene (PS) standard). Mn: number-average molecular weight, Mw: weight-average molecular weight, polydispersity: Mw/Mn. In PS calibrated GPC measurements, the actual molecular weights of aliphatic polyesters may be overestimated, depending on their structures and molecular weights [20].

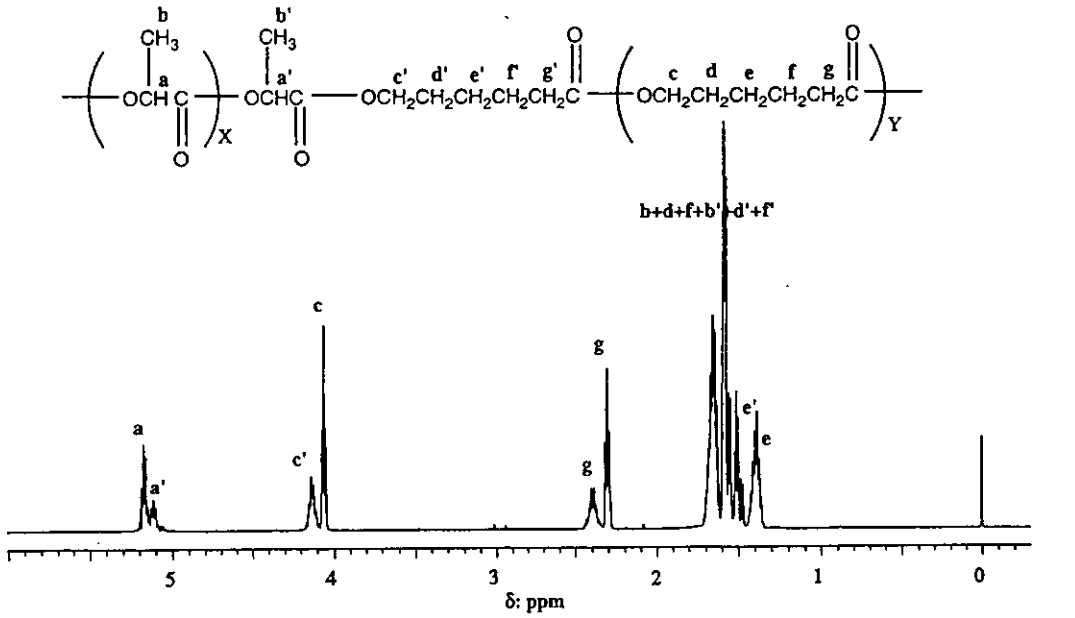

Fig. 1. ^{1}H-NMR spectrum and assignment of PLCL 50/50.

number-average molecular weight (Mn) and polydispersity (Mw/Mn) (Mw: the weight-average molecular weight) of the copolymers, determined by GPC, ranged from approximately 1.5×10^5 to 4.5×10^5 and 1.3 to 2.2, respectively. The resultant copolymers were solid except for PLCL 30/70 (30 wt% for LL and 70 wt% for CL: the designation of copolymers is given in Table 1), which is gummy.

Microfiber fabrics of good quality with different compositions of PLCL were obtained by electrospinning using MC solution at the predetermined operation conditions (Table 2). All the electrospun fabrics produced consisted of microscale fibers, ranging between approximately 4.3 and 7.0 μm in diameter, except for PLCL 30/70 which produced fused meshes probably due to its inherent physical property (gummy state) (Table 2). PLL microfibers had nanoscale pores approximately 200–800 nm in diameter at the surface and subsurface regions (Fig. 2a), which was also observed by the other research group [21]. On the other hand, such a surface structure was hardly observed for the microfiber fabrics made of the other CL-containing copolymers (Fig. 2b–e). The uniaxial tensile strength measurement test on the electrospun microfiber fabrics showed that the highest tensile strength as well as the highest Young's modulus was observed for the PLL microfiber fabric, followed by PLCL 70/30 (Fig. 3 and Table 2). Both fabrics were torn upon further elongation. PCL exhibited a relatively low Young's modulus but a high creep characteristic. The microfiber fabric

Table 2
Conditions and diameter of PLCL microfiber fabrics[a]

	Composition LL:CL	Polymer conc. in MC (wt%)	Mean diameter[b] (μm)	Young's modulus[c] (MPa)
PLL	100:0	4	4.5±0.34	17.2
PLCL 70/30	74:26	9	4.3±1.27	14.2
PLCL 50/50	50:50	7	7.0±1.03	0.8
PLCL 30/70	31:69	11	—	—
PCL	0:100	7.5	5.6±0.61	3.6

[a]Fixed electrospun conditions: flow rate, 10 ml/h; voltage, 12.5 kV; air gap, 30 cm.
[b]Measured for 20 fibers observed in scanning electron micrographs (r_{AV}±SD/μm).
[c]Young's modulus was determined from the slope in the initial linear region of the stress–strain curves of the fabrics of thickness of approximately 140 μm.

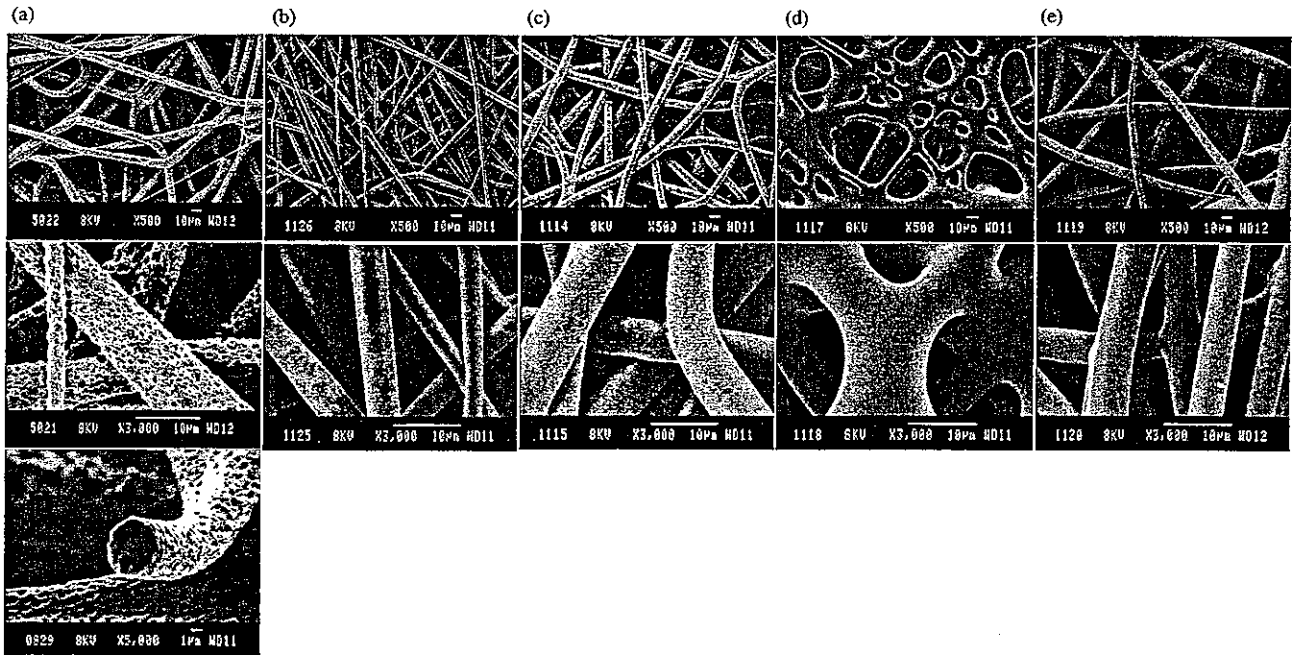

Fig. 2. SEM images of electrospun microfiber fabrics made of PLCL (co)polymers: (a) PLL, (b) PLCL 70/30, (c) PLCL 50/50, (d) PLCL 30/70, and (e) PCL.

made of PLCL 50/50 was elastomeric as shown by a low Young's modulus and an almost linear stress–strain relationship under the maximal stain (500%) in this measurement (Fig. 3 and Table 2).

3.2. Electrospun PLCL 50/50 nano- to microfiber fabrics

The mechanical strength and porosity of fabric depend on fiber composition, fiber diameter and fabric density. Nano- to microfiber fabrics were prepared using the equimolar copolymer PLCL 50/50 using different solvents under different operation conditions. This eliminates the polymer composition effect on the mechanical property and porosity of the fabrics. Table 3 shows the electrospinning conditions for the nano- to microfiber fabrics made of the copolymer. Nanoscale-fiber fabric (0.32±0.08 μm; designated fabric A) was electrospun at a concentration of 3 wt% in HFIP under a high voltage (30 kV) and a low flow rate (5 ml/h), whereas a fabric of almost 1-μm diameter fiber (1.16±0.17 μm, fabric B) was obtained at a low voltage (15 kV) and a high flow rate (10 ml/h). As described above, a fiber fabric of more than several microns in diameter (7.02±1.03 μm, fabric C) was obtained using MC solvent (Table 3). Fig. 4 shows the cross-sectional SEM images of these fabrics with a thickness of approximately 140 μm. A highly interconnected porous structure was observed, irrespective of fiber diameter.

The porosities of these fabrics with different fiber diameters were determined using a mercury intrusion

porosimeter. Fig. 5 shows the differential intrusion volume vs. pore diameter relationship on the electrospun fabrics with approximately the same thickness (140 μm), indicating that multiple peak profiles in the pore diameter ranging between ca. 0.2 and 400 μm. Regarding pore distribution, most of the pore volumes were observed in the ranges from approximately 0.2 to 30 μm (approximate mean pore diameter of 5 μm) for fabric approximately 0.2–400 μm (two peaks; approximate mean pore diameter of 80 and 40 μm) for fabric B, and approximately 1–500 μm (approximate mean pore diameter of 50 μm) for fabric C. As shown in Table 4, the calculated porosities (P_C), determined from the density of the fabrics and the density of copolymer according to the equation in the footnote of Table 4, were much higher than the porosities determined by the mercury intrusion porosimeter method. The lowest total pore volume (V_P; ml/g) and porosity (P_M), both of which were determined by the mercury intrusion porosimeter measurement, were found for fabric A. There were small significant differences in V_P and P_M between fabrics B and C, despite the fact that the density of fabric C was higher than that of fabric B.

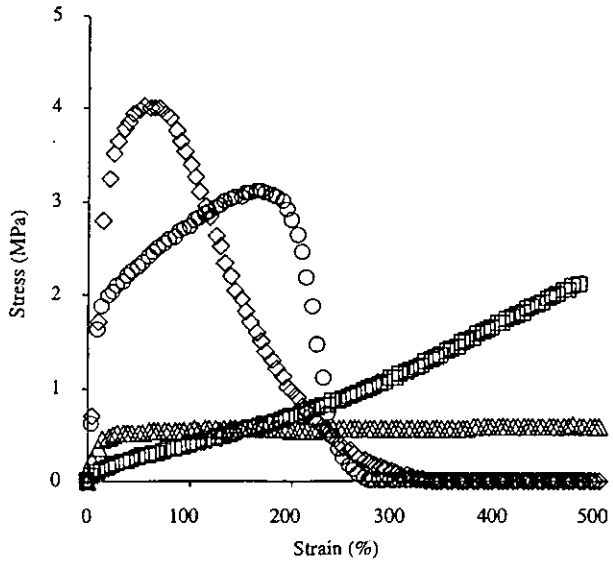

Fig. 3. Stress–strain curves for electrospun microfiber fabrics made of PLCL (co)polymers: PLL (◇), PLCL 70/30 (○), PLCL 50/50 (□), and PCL (△). Mean for $n = 4$.

Fig. 6 shows the stress–strain relationships of these nano- to microfiber fabric sheets with a thickness of approximately 140 μm (a solvent-cast film was included in comparison). Irrespective of fiber diameter, a fairly linear relationship was obtained even at 500% of strain, whereas the solvent-cast film showed a very steep linear relationship at a very low strain, followed by a creep characteristic. Young's modulus increased with a decrease in the fiber diameter of the fabric (Fig. 6 and Table 3).

3.3. Cell adhesion and proliferation potentials

The adhesion, spreading and proliferation potentials of HUVECs on fabrics made of fibers of different diameters (A, B and C in Table 3) were evaluated for 1, 4, and 7 days after seeding the cells. Cells highly elongated on fibrous meshes were observed for the fabrics made of 0.3-μm-diameter fibers (A) and 1.2-μm-diameter fibers (B) (Fig. 7). However, round or restricted-spread cells were observed on the fibers, which were quite sparsely distributed on the surface of fabric C made of 7 μm-diameter fibers. The densities of cells on the fabrics increased with incubation time for both fabrics (A and B), whereas a very low density of adhering cells on fabric C remained without any sign of proliferation even at 1-week culture (Fig. 8).

4. Discussion

The design and fabrication of scaffolds are an essential task for a functional vital engineered tissue. A provisional scaffold serves as a temporal cell adhesion and proliferation bed until natural ECM is generated by

Table 3
Electrospun PLCL 50/50 fabrics

Code name	Solvent	Polymer conc. (wt%)	Flow rate (ml/h)	Voltage (kV)	Air gap (cm)	Mean diameter[c] (μm)	Young's modulus[d] (MPa)
A	HFIP[a]	3	5	30	20	0.32±0.08	2.2
B	HFIP	3	10	15	20	1.16±0.17	1.8
C	MC[b]	7	10	13	30	7.02±1.03	0.8

[a]1,1,1,3,3,3-Hexafluoro-2-propanol (boiling point, 58 °C; dielectric constant and surface tension, 17.8 and 16.14 dyn/cm, respectively at 25 °C). (CAS No.920-66-1) [22].

[b]Methylene chloride (MC) (boiling point, 39 °C; dielectric constant and surface tension, 8.93 and 27.1 dyn/cm, respectively at 25 °C). [CAS No.75-09-2].

[c]Measured for 20 fibers observed in scanning electron micrographs (R_{AV}±SD/μm).

[d]Young's modulus was determined from the slope in the initial linear region of the stress–strain curve of the film of thickness of approximately 140 μm.

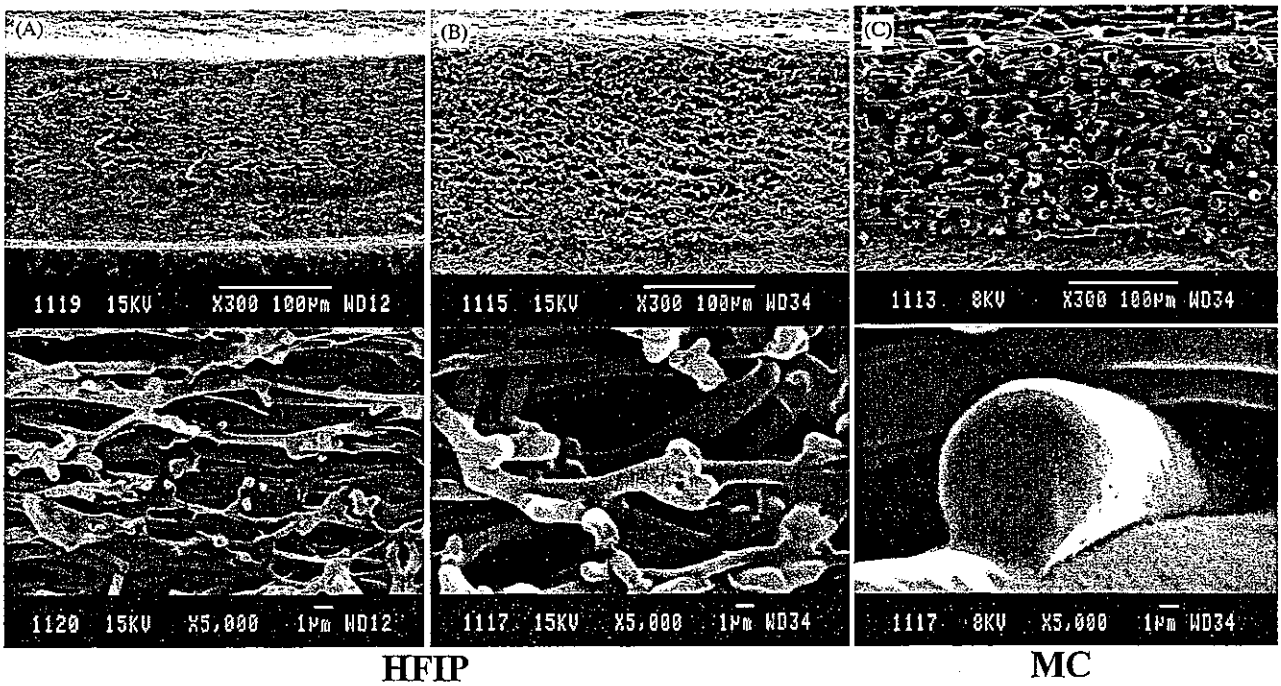

Fig. 4. SEM images of electrospun nano- to microfiber fabrics made of PLCL 50/50 copolymer. Mean diameters of fibers: (A) 0.3 μm, (B) 1.2 μm, and (C) 7 μm.

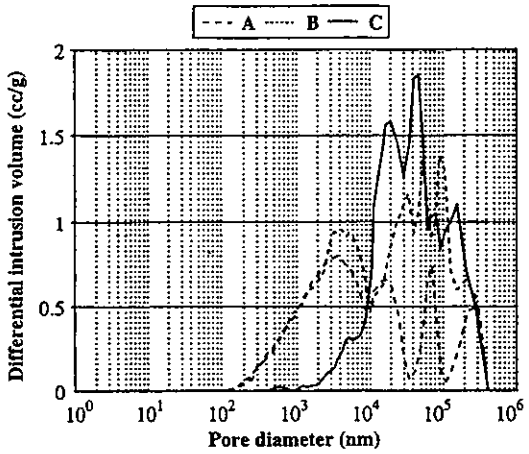

Fig. 5. Representative plots of differential intrusion volume vs. pore diameter of electrospun nano- to microfiber PLCL 50/50 fabrics. Mean diameters of fibers: (A) 0.3 μm, (B) 1.2 μm, and (C) 7 μm.

inoculated cells to form a tissue morphology resembling that of a native tissue. ECM consists of a nanoscale fibrous network of proteins and proteoglycans. Such topographical cues may have significant effects on cell behavior. To fabricate a provisional biomimetic scaffold composed of nano- to microscale fibrous meshes, electrospinning has been proven to be an effective method [11,12]. In addition to the topographical feature of a scaffold, the mechanical properties of a scaffold are another important aspect, which can be regulated by the material itself and the design of the structure. That is, a designed scaffold should not only be to provide a surface for cell residence but also to maintain sufficient biomechanical support during tissue regeneration and structure degradation. For provisional nano- or microscale fibrous meshes, biodegradable and bioabsorbable (co)poly(ester)s have been extensively studied [1,6–9]. However, a systematic study focusing on the effects of the copolymer composition and mean fiber diameter of electrospun fibrous meshes on the mechanical properties, cell adhesion and proliferation potentials has not been carried out yet.

In this study, electrospun microfiber fabrics made of a series of PLCLs with different compositions were prepared from their MC solutions. Interestingly, only PLL, which tends to exhibit a partially crystalline structure, produced nanoscale pores along the electrospun fiber surface (Fig. 2a). This phenomenon was in accordance with the experimental evidence reported by Bognitzki et al. who rationalized that the rapid phase separation induced by the evaporation of the solvent and the subsequent rapid solidification during electrospinning may be accounted for this structured surface [21]. Such nanoporous surface structuring was not observed on electrospun PLCLs and PCL microfabrics (Fig. 2b–e) [16]. Among the (co)polyesters with graded compositions (Table 1), only the equimolar copolymer PLCL 50/50 exhibited an elastomeric behavior (Fig. 3).

Table 4
Porosimetry of electrospun nano- to microfiber PLCL 50/50 fabrics[f]

Code name (mean fiber diameter)	Sample weight W/g	Sample volume V/cm^3	Density[a] D/g cm^{-3}	Calculated porosity[b] P_C/%	Porosimetry[c]	
					Total pore volume[d] V_P/ml g^{-1}	Porosity[e] P_M/%
A (0.3 μm)	0.0503	0.134	0.375	69	1.49	56
B (1.2 μm)	0.0399	0.140	0.285	76	2.29	61
C (7.0 μm)	0.0415	0.133	0.313	74	2.01	63

[a] D: weight/volume.
[b] Calculated porosity: $P_C = (1-d_m/d_p) \times 100$ (d_m: density of mesh, d_p: density of PLCL 50/50 = 1.21 g/cm^3).
[c] Measured by a mercury intrusion porosimeter.
[d] V_P: total mercury intrusion volume.
[e] Measured porosity: $P_M = V_P W\ 100/V$.
[f] Thickness: approximately 140 μm.

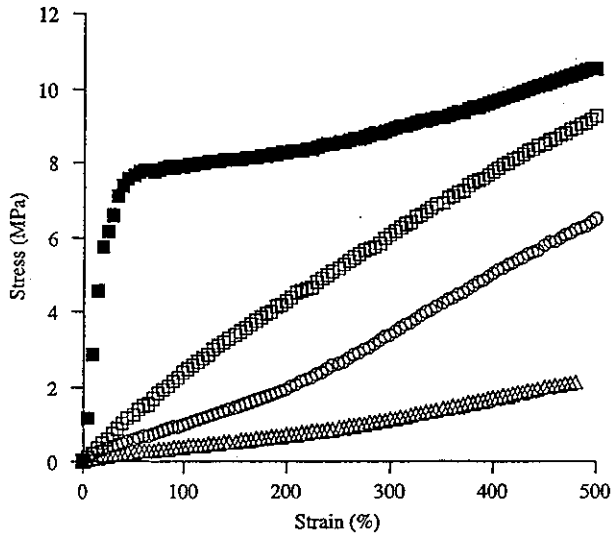

Fig. 6. Stress–strain curves for electrospun nano- to microfiber PLCL 50/50 fabrics. Mean diameter: 0.3 μm (□), 1.2 μm (○), 7 μm (△), and solvent-cast film (■). Mean for $n = 4$.

The fiber diameter of fabric made of PLCL 50/50 was controlled by the type of solvent used and operation parameters (Fig. 4: A, B, and C). As tabulated in Table 3, nanofiber fabric A, which was electrospun using HFIP (boiling point, 59 °C; dielectric constant, 17.8; and surface tension, 16.14 dyn/cm at 25 °C) as a solvent at a high applied voltage (30 kV) and a low flow rate (5 ml/h), produced a very fine fiber network (mean fiber diameter, 0.3 μm), whereas the fiber diameter produced with the same solution increased at a low applied voltage (15 kV) and a high flow rate (10 ml/h) (B: 1.2 μm). On the other hand, a microfiber fabric (C: 7.0 μm) was produced using MC (boiling point, 39 °C; dielectric constant, 8.9; and surface tension, 27.1 dyn/cm at 25 °C) using different operation parameters. Theoretically, a small fiber diameter should be obtained using a solvent having a low surface tension and a high dielectric constant under the operation conditions of a high applied voltage and a low flow rate [23]. That is, nanofibers are formed by the narrowing of the ejected jet stream as it undergoes increasing surface charge density due to evaporation of the solvent. Finer jet stream is generated by very strong electrostatic repulsion of a charged fiber surface during flight of a jet stream and subsequent burst, resulting in the formation of instable jet streams. Although the authors did not conduct a systematic approach to regulate fiber diameter, our data (Table 3) appear to follow the theoretical prediction.

As shown in Table 4 and Fig. 5, the difference in fiber diameter among the electrospun fabrics led to differences in specific density (or degree of packing of fibers), mean pore diameter and pore distribution among the fabrics. The densest fabric was found to be fabric A with the smallest fiber diameter. Both porosities (calculated and experimentally obtained), total pore volume, and mean pore diameter (approximately 5 μm; Fig. 5) were also lowest among the three fabrics (see Table 4). On the other hand, the medium-sized-fiber fabric B and large-sized-fiber fabric C had almost the same porosities (regardless of calculated or experimentally obtained one), total pore volumes and densities although the differences in mean fiber diameter were quite large (1.2 μm for B and 7.0 μm for C). Porosity can be expressed as

$$P = 1 - d_m/d_p, \tag{1}$$

which can be rewritten as

$$P = 1 - \pi r^2 L/V \tag{2}$$

since the following relation holds

$$d_m = \pi r^2 L d_p/V. \tag{3}$$

In these equations, P is porosity of fabric, d_m and d_p are densities of mesh and polymer, respectively, r is mean

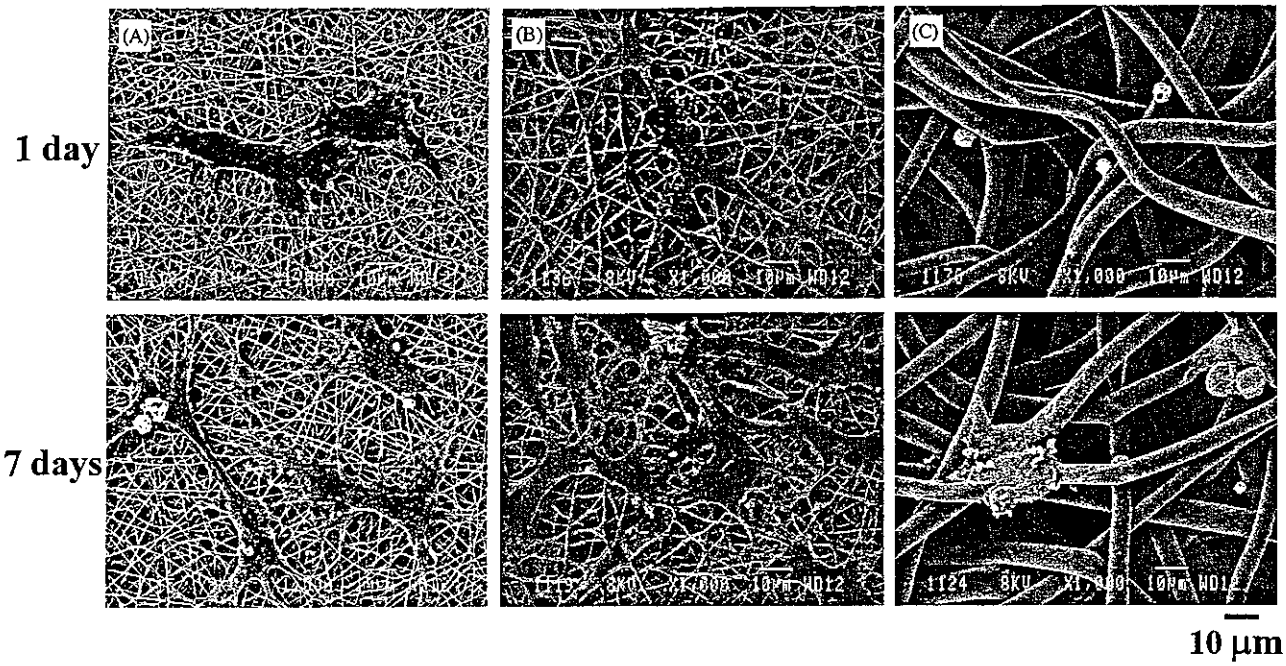

Fig. 7. SEM images of cells (HUVECs) cultured for 1 and 7 days on electrospun PLCL 50/50 fabrics with different-diameter fibers: (A) 0.3 μm, (B) 1.2 μm, and (C) 7 μm.

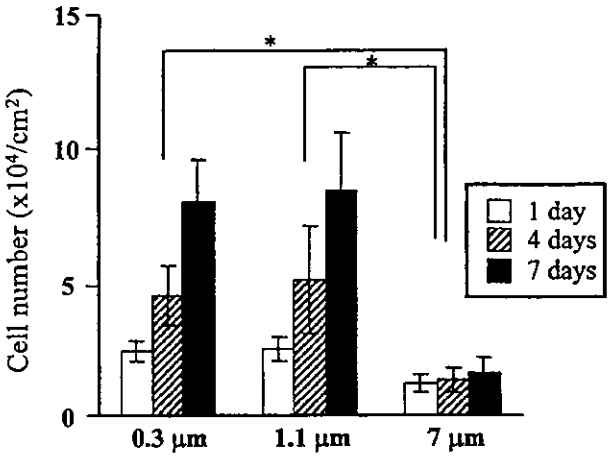

Fig. 8. Time-dependent number of cells (HUVECs) adhered on electrospun PLCL 50/50 fabrics with different-diameter fibers. Mean for $n = 4 \pm$ SD ($p < 0.05$).

radius of fiber and L/V is total fiber length (L) in the unit volume (V). Eq. (2) describes that r and L/V independently affect P. Therefore, under the condition of almost the same porosity, the exponential decrease in the fiber diameter must result in the linear increase of fiber density of fabric. This is qualitatively visualized by SEM (Fig. 4). On the other hand, the pore size distribution greatly depended on the mean fiber diameter (Fig. 5): a very high population of smaller-pore region (0.1–10 μm) and a low population of medium- to large-sized-pore region (10–400 μm) were observed for the highest dense fabric A, whereas the least dense fabric C had few small-sized pores but many large-sized pores. The intermediately dense fabric B exhibited a biphasic pore-distribution characteristic of these two high and low fiber density-fabrics.

The mechanical properties of non-woven fabrics depend on geometrical structures of fibers [24]. The highest Young's modulus was observed for highest dense fabric A, followed by that of fabric B and the lowest Young's modulus was observed for least dense fabric C at almost the same porosity or density (Fig. 6 and Table 3). This indicates that a decrease in the fiber diameter of fabric increases mechanical strength probably due to the increase of the fiber density.

As for the behavior of cells on the fabrics, the higher cell adhesion and proliferation potential of HUVECs were noted on both the small- and medium-sized-fiber fabrics (A and B) compared with fabric C (Figs. 7 and 8). The numbers of fibers existing at the unit area of outermost surfaces of the fabrics, determined from the SEM images (40 μm × 40 μm; $n = 4$), were as follows: $40.5 \pm 4.5/1600\ \mu m^2$ for fabric A, $15.1 \pm 2.2/1600\ \mu m^2$ for fabric B and $2.5 \pm 0.6/1600\ \mu m^2$ for fabric C. The surface of the dense fabric eventually enabled the adhesion, spreading and proliferation of cells which anchored on many fibers at the outermost surface, as observed in fabrics (A and B) (Figs. 7 and 8). On the other hand, the most sparsely distributed fabric with the largest

diameter (fabric C) provided quite different types of cell behavior: cells adhered on a single fiber are round-shaped and non-proliferating cells predominated. Such behaviors should result from a large interfiber distance or a very low surface density of fibers, which did not permit cell adhesion across the neighboring fibers.

There has been an increasing interest in nanoscale fibrous synthetic scaffolds associated with the biomimicking of the basement membrane which shows a nano- to submicron-scale topography of extracellular matrix macromolecules, including fiber meshes [6–9], pores [25], ridges [26], grooves [26], and peak valleys [27]. Among nanoscale biodegradable synthetic polymers, (co)poly(ester)s such as PLL, poly(lactide-*co*-glycolide) (PLGA), PCL and PLCL have been fabricated into nanofibers by electrospinning [6–9,21]. Cell adhesiveness and proliferability on these fabrics were reported, and the potential applications for tissue engineering based upon its unique architecture, which serves to support and guide cell growth were discussed [6–9]. Highly packed fabrics or high-surface-density fibers provide an extremely high surface-to-volume ratio, which favors cell attachment and proliferation [8]. The results of our present study agreed very well with those of previous studies. Taken together with the results obtained in this study, a more functional biodegradable polymer-based "bioactive" and "mechano-active" tubular scaffold for vascular tissue replacement technology will be reported in the near future.

5. Conclusion

Highly interconnected porous nano- to microfiber fabrics made of PLCL copolymers with different compositions were electrospun. Different fabric architectures of the elastomeric copolyester, the equimolar PLCL copolymer, were prepared using different solvents. The decrease in the fiber diameter of fabric resulted in a decrease in porosity and pore size, but an increase in fiber density and mechanical strength. HUVECs were well adhered and proliferated on the highly packed nano- and 1-micron-scaled-fiber fabrics. The discussion suggests that electrospun elastomeric nanofiber fabric thus prepared may be useful as provisional functional scaffolds in cardiovascular and muscular tissue engineerings.

Acknowledgements

The authors thank Dr. T. Kanemaru of the Faculty of Medicine, Kyushu University, for SEM. This study was financially supported in part by a Grant-in-Aid for Scientific Research (A2-15200038) from Ministry of Education, Culture, Sports, Science, and Technology (MEXT), Japan.

References

[1] Mikos AG, Bao Y, Cima LG, Ingber DE, Vacanti JP, Langer R. Preparation of PGA bonded fibre structure for cell attachment and transplantation. J Biomed Mater Res 1993;27:183–9.
[2] Park A, Wu B, Griffith LG. Integration of surface modification and 3D fabrication techniques to prepare patterned poly (L-lactide) substrates allowing regionally selective cell adhesion. J Biomater Sci Polym Ed 1998;9:89–110.
[3] Kwon IK, Park KD, Choi SW, Lee SH, Lee EB, Na JS, Kim SH, Kim YH. Fibroblast culture on surface-modified poly(glycolide-*co*-ε-caprolactone) scaffold for soft tissue regeneration. J Biomater Sci Polym Ed 2001;12:1147–60.
[4] Elsdale T, Bard J. Collagen substrata for studies on cell behavior. J Cell Biol 1972;54:626–37.
[5] Curtis ASG, Riehle MO. Tissue engineering: the biophysical background. Phys Med Biol 2001;46:47–65.
[6] Li WJ, Laurencin CT, Caterson EJ, Tuan RS, Ko FK. Electrospun nanofibrous structure: a novel scaffold for tissue engineering. J Biomed Mater Res 2002;60:613–21.
[7] Yoshimoto H, Shin YM, Terai H, Vacanti JP. A biodegradable nanofibers scaffold by electrospinning and its potential for bone tissue engineering. Biomaterials 2003;24:2077–82.
[8] Mo XM, Xu CY, Kotaki M, Ramakrishna S. ElectrlspunP(LLA-CL) nanofiber: a biomimetic extracellular matrix for smooth muscle cell and endothelial cell proliferation. Biomaterials 2004;25:1883–90.
[9] Reneker DH, Kataphinan W, Theron A, Zussman E, Yarin AL. Nanofiber garlands of polycaprolactone by electrospinning. Polymer 2002;43:6785–94.
[10] Matthews JA, Wnek GE, Simpson DG, Bowlin GL. Electrospinning of collagen nanofibers. Biomacromolecules 2002;3:232–8.
[11] Reneker DH, Chun I. Nanometre diameter fibres of polymer, produced by electrospinning. Nanotechnology 1996;7:216–23.
[12] Shin YM, Hohman MM, Brenner MP, Rutledge GC. Experimental characterization of electrospinning: the electrically forced jet and instabilities. Polymer 2001;42:9955–67.
[13] de Groot JH, Zijlstra FM, Kuipers HW, Pennings AJ, Klompmaker J, Veth RP, Jansen HW. Meniscal tissue regeneration in porous 50/50 copoly(L-lactide/epsilon-caprolactone) implants. Biomaterials 1997;18:613–22.
[14] den Dunnen WF, van der Lei B, Robinson PH, Holwerda A, Pennings AJ, Schakenraad JM. Biological performance of a degradable poly(lactic acid-epsilon-caprolactone) nerve guide: influence of tube dimensions. J Biomed Mater Res 1995;29:757–66.
[15] Kricheldorf HR, Kreiser-Saunders I, Boettcher C. Polylactones: 31. Sn(II)octoate-initiated polymerization of L-lactide: a mechanistic study. Polymer 1995;36:1253–9.
[16] Hiljanen-Vainio M, Karjalainen T, Seppälä J. Biodegradable lactone copolymers I. Characterization and mechanical behavior of ε-caprolactone and lactide copolymer. J Appl Polym Sci 1996;59:1271–88.
[17] Grijpma DW, Zondervan GJ, Pennings AJ. High molecular weight copolymers of L-lactide and ε-caprolactone as biodegradable elastomeric implant material. Polym Bull 1991;25:327–34.
[18] Kidoaki S, Kwon IK, Matsuda T. Mesoscopic spatial designs of nano- and microfiber meshes for tissue-engineering matrix and scaffold based on newly devised multilayering and mixing electrospinning techniques. Biomaterials 2005;26:37–46.

[19] Washburn EW. Note on a method of determining the distribution of pore sizes in a porous material. Proc Natl Acad Sci USA 1921;7:115–6.
[20] Pasch H, Rode K. Use of matrix-assisted laser desorption/ionization mass spectrometry for molar mass-sensitive detection in liquid chromatography of polymers. J Chromatography A 1995;699:21–9.
[21] Bognitzki M, Czado W, Frese T. Nanostructured fibers via electrospinning. Adv Mater 2001;13:70–2.
[22] Fioroni M, Burger K, Mark AE, Roccatano D. Model of 1,1,1,3,3,3-Hexafluoro-propan-2-ol for molecular dynamics simulations. J Phys Chem B 2001;105:10967–75.
[23] Ma PX, Choi JW. Biodegradable polymer scaffolds with well-defined interconnected spherical pore network. Tissue Eng 2001;7: 23–33.
[24] Lee KH, Kim HY, La YM, Lee DR, Sung NH. Influence of a mixing solvent with tetrahydrofuran and *N,N*-dimethylformamide on electrospun poly(vinyl chloride) Nonwoven mats. J Polym Sci Part B: Polym Phys 2002;40: 2259–68.
[25] Campbell CE, von Recum AF. Microtopography and soft tissue response. J Invest Surg 1989;2:51–74.
[26] den Braber ET, de Ruijter JE, Smits HTJ, Ginsel LA, von Recum AF, Jansen JA. Quantitative analysis of fibroblast morphology on microgrooved surfaces with various groove and ridge dimensions. Biomaterials 1996;17:2037–44.
[27] Dalby MJ, Riehle MO, Johnstone H, Affrossman S, Curtis ASG. In vitro reaction of endothelial cells to polymer demixed nanotopography. Biomaterials 2002;23:2945–54.

Available online at www.sciencedirect.com
SCIENCE DIRECT®
Biomaterials 25 (2004) 3117–3123
Biomaterials
www.elsevier.com/locate/biomaterials

Antisense oligonucleotides bound in the polysaccharide complex and the enhanced antisense effect due to the low hydrolysis ☆

Masami Mizu[a], Kazuya Koumoto[a], Takahisa Anada[a], Kazuo Sakurai[a,*], Seiji Shinkai[b]

[a] *Department of Chemical Process & Environments, The University of Kitakyushu, 1-1, Hibikino, Wakamatu-ku, Kitakyushu, Fukuoka 808-0135, Japan*
[b] *Faculty of Engineering Department of Chemistry & Biochemistry, Graduate School of Engineering, Kyushu University, 6-10-1 Hakozaki, Higashi-ku, Fukuoka, Fukuoka 812-8581, Japan*

Received 2 July 2003; accepted 10 November 2003

Abstract

Schizophyllan is a β-(1→3)-D-glucan and can form a novel complex with some single-chains of DNAs. As the preceding paper revealed, the polynucleotide bound in the complex is more stable to nuclease-mediated hydrolysis than the polynucleotide itself (i.e., naked polynucleotide). This paper examined possibility to apply this complex to an antisense DNA carrier, using an in vitro (cell-free) transcription/translation assay. In this assay, we used a plasmid DNA coding a green fluorescence protein (GFP) and an antisense DNA designed to hybridize the ribosome-binding site in the GFP-coded mRNA. When the antisense DNA was administered as the complex, a lower GFP expression efficiency (or higher antisense effect) is observed over naked DNA. This is because the antisense DNA in the complex is protected from the attack of deoxyribonuclease. When exonuclease I, which specifically hydrolyzes single DNA chains, was present in the GEP assay system, the antisense effect was not changed for the complex while being weakened in the naked antisense DNA system. These results imply that the exonuclease I cannot hydrolyze the antisense DNA in the complex, while it can hydrolyze naked DNA to reduce its antisense effect.

Keywords: Antisense; DNA; Gene expression; Polysaccharide; Complexation

1. Introduction

Schizophyllan is an extracellular polysaccharide produced by the fungus *Schizophyllan commune* and the main chain consists of β-(1→3)-D-glucan and one β-(1→6)-D-glycosyl side chain links to the main chain at every three glucose residues [1]. Schizophyllan adopts a triple helix conformation in water and a random coil in dimethylsulfoxide (DMSO) [2,3]. When water is added to the DMSO solution (renaturation), the triple helical structure can be partially retrieved through this process, although the entire chain structure may not be the same with the original triple helix [4,5]. Recently, Sakurai and Shinkai [6,7] found that the schizophyllan single chain (s-SPG[1]) forms a macromolecular complex with some homo-polynucleotides, when the polynucleotide is present in the renaturation process. Their subsequent paper [8] reveals that the polynucleotide bound in the complex is more stable to nuclease-mediated hydrolysis than the polynucleotide itself (i.e., naked polynucleotide), using both high-performance liquid chromatography and ultraviolet absorbance methods. This low hydrolysis of the complex suggests that s-SPG is applicable to an antisense oligonucleotide (AS ODN) carrier.

In this paper, we attempted to further evaluate the capability of the complex to act as an AS ODN carrier, using the pQBI63 vector as a reporter gene in *Escherichia coli* T7 S30 extract solutions. The pQBI63 vector contains the gene to code a red-shifted green fluorescence protein [9–11] (hereinafter we simply call it GFP) and the GFP-coding region is under the control of a T7 promoter [11]. Since the *E. coli* T7 S30 extract solution contains the T7 RNA polymerase, essential amino acids, and other all necessary components for translation, once the pQBI63 was added to the extract solution, the GFP-coding mRNA is produced, and subsequently GFP is produced. This system is called "in vitro cell-free transcription/translation assay" and

☆ This paper is the 20th paper in the series of polysaccharide/polynucleotide complexes.

* Corresponding author.
E-mail address: sakurai@env.kitakyu-u.ac.jp (K. Sakurai).

[1] In this paper, s-SPG and t-SPG stand for single chain of schizophyllan and natural triple helix of schizophyllan, respectively.

0142-9612/$ - see front matter © 2003 Elsevier Ltd. All rights reserved.
doi:10.1016/j.biomaterials.2003.11.008

have been shown very useful for antisense assays [12–14]. We applied this established assay method to our s-SPG complex to evaluate how the complex enhances the antisense effect.

2. Experimental

2.1. Materials

Taito Co. Ltd. (Japan) kindly supplied a fractionated triple-helix schizophyllan sample. The weight-average molecular weight (M_w) and the number of repeating units were found to be 1.5×10^5 and 231, respectively [6,7]. Polyethyleneimine (PEI) with 80 kDa (Fluka), dextran ($M_w = 10^5$) (Wako), and amylose ($M_w = 2800$) (Wako) were used without further purification. *E. coli* SK4258 originated exonuclease I (Exonuclease I) was purchased from Pharmacia. The pQBI63 vector was purchased from Takara, and the *E. coli* T7 S30 extract solutions were purchased from Promega [12] and Novagen [15]. The antisense sequence (CTTTAAGAAGGAGATATACAT) was used to hybridize the ribosome binding site (the antisense of binding site is underlined, see Table 1) [13,16]. We found that s-SPG cannot bind the antisense sequence itself, because of the short sequence length [17]. Since we already knew that a certain length of poly(dA) is necessary to bind to s-SPG [17], we added a poly(dA) tail [poly(dA)$_{20}$ or poly(dA)$_{40}$] to the end of the antisense sequence as shown in Table 1 and used four different AS ODN samples (denoted by ANT1, ANT2, ANT3 and ANT4). All AS ODN samples were synthesized at Hokkaido System Science (Japan).

2.2. DNA complexation

50 μg of each ANT sample (i.e., ANT1, ANT2, ANT3 and ANT4) was dissolved in 10 mM Tris buffer (pH 8.0) containing 50 mM KCl. A s-SPG/DMSO solution with an appropriate concentration was added to each ANT solution so that the water volume fraction was always 0.9 after mixing. In most cases, the molar ratio ($M_{s\text{-}SPG}/M_{ANT}$) was controlled to 1.0, where $M_{s\text{-}SPG}$ and M_{ANT} are the repeating molar concentrations of s-SPG and ANT, respectively. Only for ANT1, $M_{s\text{-}SPG}/M_{ANT}$ was changed to 0.1, 0.25, 0.5, 0.75, 1.0, 2.0, 3.0, and 4.0 in order to optimize experimental conditions. After the s-SPG+ANT[2] mixture was left at 5°C for 24 h to allow the complex to form, DMSO was removed by ultra-filtration (3000 M_w cut off, Millpore). After filtration, the final concentration of ANT was determined by ultraviolet absorbance.

[2] In this paper, s-SPG+ANT stands for a mixture of ANT and s-SPG, and does not necessary mean the complex. This can be just a mixture of the two components without any complexation. In fact, s-SPG+ANT2 does not form a complex. However, the ANT1, ANT3 and ANT4 mixtures essentially only consist of s-SPG/ANT complexes [8].

Table 1
AS ODN samples and their sequences used in this study

Name	Sequence	Size (bases)
Antisense	CTTTAAGAAGGAGATATACAT	21
ANT1	CTTTAAGAAGGAGATATACAT-dA$_{40}$	61
ANT2	dA$_{20}$-CTTTAAGAAGGAGATATACAT-dA$_{20}$	61
ANT3	dA$_{40}$-CTTTAAGAAGGAGATATACAT-dA$_{40}$	101
ANT4	dA$_{40}$-CTTTAAGAAGGAGATATACAT	61

The binding site is underlined, which is designed to hybridize the ribosome binding site of the T7 promoter system [13,14,16].

The preceding paper [8] employed gel electrophoresis and spectroscopic methods to show that s-SPG can form complexes with both ANT1 and ANT2, while ANT3 cannot. This difference in the complexation ability is ascribed to differences in the length of the poly(dA) tail [17]. We did not directly examine whether ANT4 forms the complex since ANT4 has the considered poly(dA)$_{40}$ tail on its 5′ end.

2.3. In vitro transcription/translation assay

A known in vitro cell-free transcription/translation assay was performed, using the pQBI63 vector in *E. coli* T7 S30 extract solutions (Promega or Novagen). The pQBI63 was amplified in *E. coli BL21(DE3)* (Novagen) and purified with a Plasmid Midi Kit (Qiagen). 1 μg of pQBI63 plasmid was added to 50 μl of the *E. coli* T7 S30 extract solution and the resultant solution was incubated at 37°C. In this condition, after 30 min, the plasmid DNA (i.e., pQBI63) started to express a sufficient amount of GFP, enough to provide appreciable fluorescence intensity. We adopted this protocol as the standard. To evaluate ANT/carrier antisense effects, the ANT samples or their s-SPG complexes were added to the standard. Usually, 10 μg of ANT was added to the standard. The total amount of the carrier complex was changed so as to maintain 10 μg of total ANT in an assay. The amount of GFP expressed was evaluated as the fluorescence intensity at 507 nm (excited at 463 nm) with a Hitachi F4500 fluorescence spectrometer.

According to Promega Technical Notes [18], "linearization significantly reduces the expression of the luciferase gene in the T7 S30 system. This reduction is a result of exonuclease activity in the T7 S30 system". Therefore, Promega's *E. coli* T7 S30 extract solution contains some amount of nuclease. This situation is convenient to examine how the s-SPG/ANT complex protects the bound AN ODNs from nuclease-mediated hydrolysis. Thus, we decided to compare antisense